JCI insight

RESEARCH ARTICLE

Endothelial SOCS3 maintains homeostasis and promotes survival in endotoxemic mice

Nina Martino,[1] Ramon Bossardi Ramos,[1] Shuhan Lu,[1] Kara Leyden,[1] Lindsay Tomaszek,[1] Sudeshna Sadhu,[1] Gabrielle Fredman,[1] Ariel Jaitovich,[1,2] Peter A. Vincent,[1] and Alejandro P. Adam[1,3]

[1]Department of Molecular and Cellular Physiology, [2]Division of Pulmonary and Critical Care Medicine, and [3]Department of Ophthalmology, Albany Medical Center, Albany, New York, USA.

SOCS3 is the main inhibitor of the JAK/STAT3 pathway. This pathway is activated by interleukin 6 (IL-6), a major mediator of the cytokine storm during shock. To determine its role in the vascular response to shock, we challenged mice lacking SOCS3 in the adult endothelium ($SOCS3^{iEKO}$) with a nonlethal dose of lipopolysaccharide (LPS). $SOCS3^{iEKO}$ mice died 16–24 hours postinjection after severe kidney failure. Loss of SOCS3 led to an LPS-induced type I IFN–like program and high expression of prothrombotic and proadhesive genes. Consistently, we observed intraluminal leukocyte adhesion and neutrophil extracellular trap–osis (NETosis), as well as retinal venular leukoembolization. Notably, heterozygous mice displayed an intermediate phenotype, suggesting a gene dose effect. In vitro studies were performed to study the role of SOCS3 protein levels in the regulation of the inflammatory response. In human umbilical vein endothelial cells, pulse-chase experiments showed that SOCS3 protein had a half-life less than 20 minutes. Inhibition of SOCS3 ubiquitination and proteasomal degradation led to protein accumulation and a stronger inhibition of IL-6 signaling and barrier function loss. Together, our data demonstrate that the regulation of SOCS3 protein levels is critical to inhibit IL-6–mediated endotheliopathy during shock and provide a promising therapeutic avenue to prevent multiorgan dysfunction through stabilization of endothelial SOCS3.

Introduction

Systemic inflammatory response syndrome (1) often leads to multiorgan dysfunction (MODS) through an acute release of cytokines, in a process often called cytokine storm (2). The release of these cytokines mediates the vascular dysfunction leading to shock, including refractory vasodilation, microvascular thrombosis, leukocyte plugging, and increased vascular permeability. These defects lead to systemic hypotension, organ hypoperfusion, and ultimately organ failure and death (3–6). These phenomena are mainly driven by the host's immune response through a mechanism that involves, at least in part, cytokine-induced vascular dysfunction (3, 7). The circulating levels of the proinflammatory cytokine interleukin 6 (IL-6) correlate with disease severity (8–12) and are highly predictive of mortality (13, 14). In fact, an IL-6 amplifier mechanism that consists of a positive feedback regulation of this cytokine has been linked to worse prognosis (9). IL-6 binds to a heterodimeric receptor consisting of a transmembrane glycoprotein 130 (gp130) subunit that is responsible for signal transduction and a smaller IL-6 receptor α (IL-6Rα), or gp80 subunit, that presents the cytokine to gp130 (9, 15). Very few cells express gp80, but a soluble form (sIL-6Rα) quickly appears in circulation during inflammation and presents the ligand to gp130 to activate its downstream signaling, in a process termed "trans-signaling" (9, 15). Upon ligation, this receptor activates the Janus tyrosine kinases (JAKs) to induce several downstream signal transduction cascades, including the activation of signal transduction and activator of transcription 3–dependent (STAT3-dependent) gene expression through its phosphorylation on tyrosine 705 (9, 16). Multiple positive and negative feedback loops regulate the intensity and duration of this signal. Chiefly, STAT3-mediated expression of SOCS3 leads to a potent negative regulation. SOCS3 binds to the gp130/JAK complex to block further STAT3 phosphorylation (17–20).

The direct effects of IL-6 on the endothelium are not completely understood. Moreover, the role for its downstream signaling in promoting shock-induced endotheliopathy is still unclear. Activation of this pathway leads to an increase in expression of leukocyte binding molecules (such as ICAM, E selectin, and P selectin) at the surface of the endothelium and a decrease in antithrombotic proteins (21). Many reports point to a role for IL-6 in promoting vascular leak in vivo (15, 22–25). Using in vitro models, we (26) and others (27–30) have shown that IL-6 directly promotes increases in endothelial permeability. In human umbilical vein endothelial

Conflict of interest: The authors have declared that no conflict of interest exists.

Submitted: December 29, 2020
Accepted: June 16, 2021
Published: June 17, 2021

Reference information: *JCI Insight*. 2021;6(14):e147280. https://doi.org/10.1172/jci.insight.147280.

cells (HUVECs), IL-6–induced increase in endothelial permeability is sustained for prolonged periods, which conflicts with the notion of a strong negative regulation via STAT3-induced SOCS3 expression. This barrier function loss requires STAT3 phosphorylation at tyrosine 705 and de novo protein synthesis (26). The transcriptional response in the endothelium leading to vascular leak, however, is not known.

Here, we sought to determine the role of SOCS3 in the regulation of the intensity and duration of IL-6 signaling in the endothelium by assessing the response to endotoxin in mice lacking SOCS3 specifically in the adult endothelial cells (SOCS3^{iEKO}). We found that SOCS3 deletion led to fast mortality less than 24 hours after an endotoxin injection that was nonlethal in control mice. Surviving SOCS3^{iEKO} mice 16 hours postchallenge showed severe kidney failure, accumulation of intraluminal leukocytes in multiple organs, vascular leakage, and a prothrombotic and an adhesive transcriptional response that was associated with a strong induction of type I IFN–regulated genes. Notably, heterozygous mice displayed an intermediate phenotype, suggesting a gene dose effect. In vitro, we demonstrate that the sustained barrier function loss induced by an IL-6 treatment can be explained by fast SOCS3 ubiquitination and proteasomal degradation that prevents sufficient protein accumulation to act as an effective barrier to this pathway. Together, these findings demonstrate a crucial role for the regulation of endothelial SOCS3 levels to minimize vascular dysfunction and uncover a promising and potentially novel therapeutic target for balancing an uncontrolled inflammatory response.

Results

SOCS3^{iEKO} mice die within 24 hours after endotoxin challenge. To determine the role of endothelial SOCS3 in the vascular response to inflammation, we generated tamoxifen-inducible, endothelial specific SOCS3-knockout mice (herein, SOCS3^{iEKO}). For that purpose, we crossed SOCS3$^{fl/fl}$ with mice carrying a cdh5-CreER^{T2} inducible endothelial Cre driver. A tdTomato reporter was also introduced. Control mice carried the Cre driver and tdTomato reporter but WT SOCS3 alleles. All mice were treated with tamoxifen for 5 consecutive days. Upon tamoxifen treatment, SOCS3^{iEKO} displayed a deletion of part of exon 2 (Figure 1A). Flow cytometry of cells obtained from the lung, a highly vascularized tissue, showed that approximately 50% of cells were positive for tdTomato, while the fraction of cells positive in blood or in bone marrow was much lower (Figure 1B). Moreover, Quantitative reverse-transcription PCR (RT-qPCR) of CD45^{+} cells obtained from spleen (Supplemental Figure 1; supplemental material available online with this article; https://doi.org/10.1172/jci.insight.147280DS1) demonstrates a lack of SOCS3 excision in these cells (Figure 1C), suggesting a low activity of this Cre driver in hematopoietic cells, a finding that is consistent with other reports (31). Mice were viable for several weeks postexcision, without any obvious phenotype. Then, we challenged SOCS3^{iEKO}, control, and heterozygous littermate controls 2 weeks postexcision with a single dose of endotoxin (250 μg/mouse of lipopolysaccharides from *E. coli* 0111:B4, LPS) or saline solution. As shown in Figure 1D, a dose of LPS that was not lethal in WT mice led to a very fast mortality in the SOCS3 knockouts. All LPS-treated SOCS3^{iEKO} mice died by 24 hours, with death starting at approximately 16 hours posttreatment. To better understand the mortality in these mice, we developed a set of objective criteria based on recently described scoring systems for similar conditions, with small modifications (32–34) (described in Supplemental Table 5). As expected, endotoxemic mice showed an increased severity score, which was further aggravated by the SOCS3 deficiency (Figure 1E). Notably, even though all heterozygous littermates survived, they received an intermediate severity score, suggesting that loss of a single SOCS3 allele is sufficient to worsen the inflammatory response (Figure 1E). Further, LPS-induced hypothermia was much more pronounced in SOCS3^{iEKO} mice, again with heterozygous mice having intermediate values (Figure 1F).

We had hypothesized that a loss of endothelial SOCS3 expression might mimic the effects of an IL-6 amplifier loop (9), leading to an overactivated pathway that would be associated with a worse outcome. Thus, we directly tested whether SOCS3^{iEKO} mice displayed increased IL-6 expression and signaling. In fact, we detected a dramatic increase in whole-tissue IL-6 mRNA levels in lungs, kidneys, and livers of these mice (Figure 2A), as well as an increase in SOCS3 mRNA itself (Figure 2B). Given that the SOCS3 primers were designed to detect full-length but not deleted SOCS3 mRNA, we speculate that nonendothelial cell types are responsible for this increase. Consistently, knockout mice showed substantially increased levels of circulating IL-6, an effect that was not apparent when looking at the circulating TNF-α (Figure 2C).

Endotoxemic SOCS3^{iEKO} mice have increased vascular permeability and multiple organ dysfunction. After the endotoxin challenge, all mice showed weight loss; however, SOCS3^{iEKO} mice consistently lost less weight than their control littermates (Figure 3A). Liquid retention is a hallmark of severe shock. Thus, we hypothesized that this reduced weight loss in SOCS3^{iEKO} mice might be due to increased edema caused

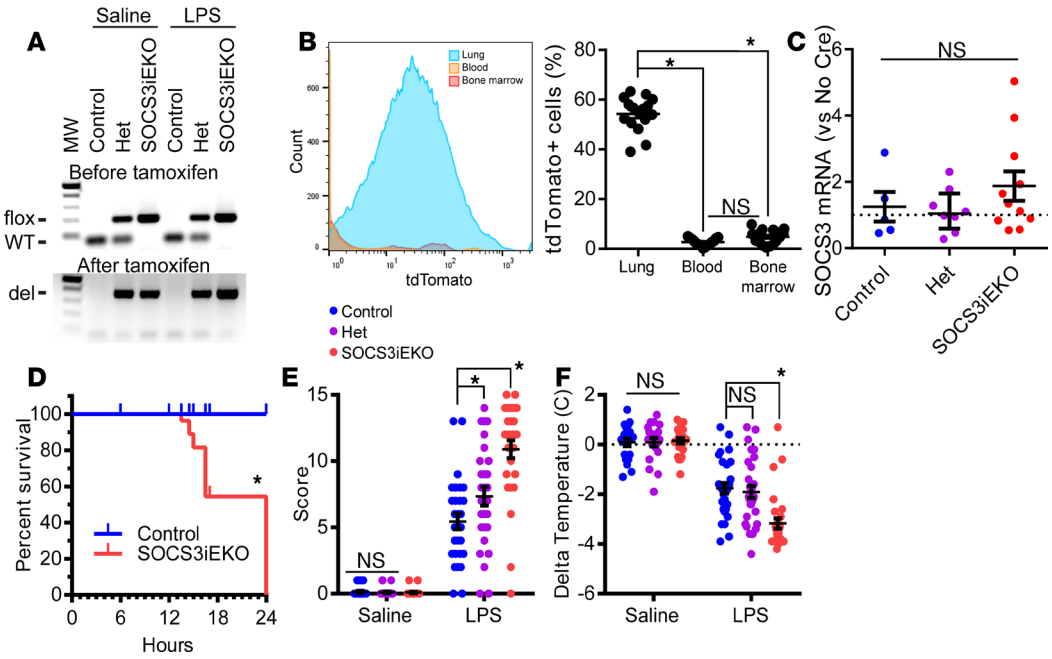

Figure 1. Loss of endothelial SOCS3 dramatically increases the severity of the response to endotoxin. (**A**) Sample genotyping before and after tamoxifen addition confirming the deletion of SOCS3. (**B**) Flow cytometry analysis of tomato expression showing only a minor expression in circulating and bone marrow cells and in a large proportion of lung cells, suggesting high selectivity and penetrance of Cre activation (n = 15–16). (**C**) RT-qPCR of CD45$^+$ cells showing similar levels of SOCS3 expression in WT and SOCS3^{iEKO} mice after tamoxifen treatment (Kruskal-Wallis). activation (n = 5-11.) (**D**) Survival curve of mice challenged with a single dose of 250 μg of endotoxin via intraperitoneal injection. Marks denote censored animals (those that were removed for diverse measurements) (Kaplan-Meier analysis, n = 30-37). (**E**) Severity score of mice 15–16 hours after saline or LPS injection (2-way ANOVA with Dunnett's post hoc test, het or SOCS3^{iEKO} vs. control). (n = 20–29.) (**F**) Temperature difference for each mouse as measured immediately before and 15–16 hours postinjection (2-way ANOVA with Dunnett's post hoc test, het or SOCS3^{iEKO} vs. control). (n = 20–29.) Asterisks denote $P < 0.05$. Data combined from at least 3 independent experiments.

by systemic vascular leak. To assess whether loss of SOCS3 increased vascular leak, we injected LPS- or saline-treated mice with FITC-dextran (70 kDa), allowed it to circulate for 30 minutes, and then euthanized the mice and perfused them with PBS. Little dextran leaked from brain (Figure 3B) or lungs (Figure 3C) of control mice 15 hours after LPS. However, dextran leak was evident in multiple spots in the organs of similarly treated SOCS3^{iEKO} mice (Figure 3, B and C), demonstrating that loss of SOCS3 promoted a modest increase in vascular leak after endotoxin. The leak was particularly noticeable around vessels in the brain cortex and in the lung periphery.

To better understand the mechanisms of lethality in SOCS3^{iEKO} mice, we performed a series of experiments aimed at determining the extent of organ dysfunction. Measurement of blood glucose showed that endotoxin promoted a severe hypoglycemia independent of mouse genotype (Figure 4A). Surprisingly, lactate levels 15 hours after endotoxin challenge were lower in endotoxin- than in saline-treated mice. We attributed this finding to the severe hypoglycemia, which would limit the available source for the glycolysis needed for lactate generation. However, SOCS3^{iEKO} mice showed increased lactate levels compared with control endotoxemic mice, despite similar low glycemia (Figure 4B), suggesting higher glycolysis that may be due to increased hypoxia. Although we found a very mild lung infiltration in endotoxemic mice, loss of SOCS3 did not aggravate the histological findings (Figure 4C). Masked scoring of lung damage demonstrated no significant differences between control and SOCS3^{iEKO} (median = 1 for both groups; score range from 1, normal, to 4, severe pathology) endotoxemic mice. Moreover, O_2 saturation values higher than 96% at room air were consistently recorded on all animals even at an advanced stage of acute illness (Figure 4D), suggesting that lung injury cannot explain these findings.

Liver glycogen content was severely reduced in endotoxemic mice (Supplemental Figure 2A). However, plasma albumin levels remained constant among experimental groups (Supplemental Figure 2B), suggesting that liver dysfunction is very limited in this model.

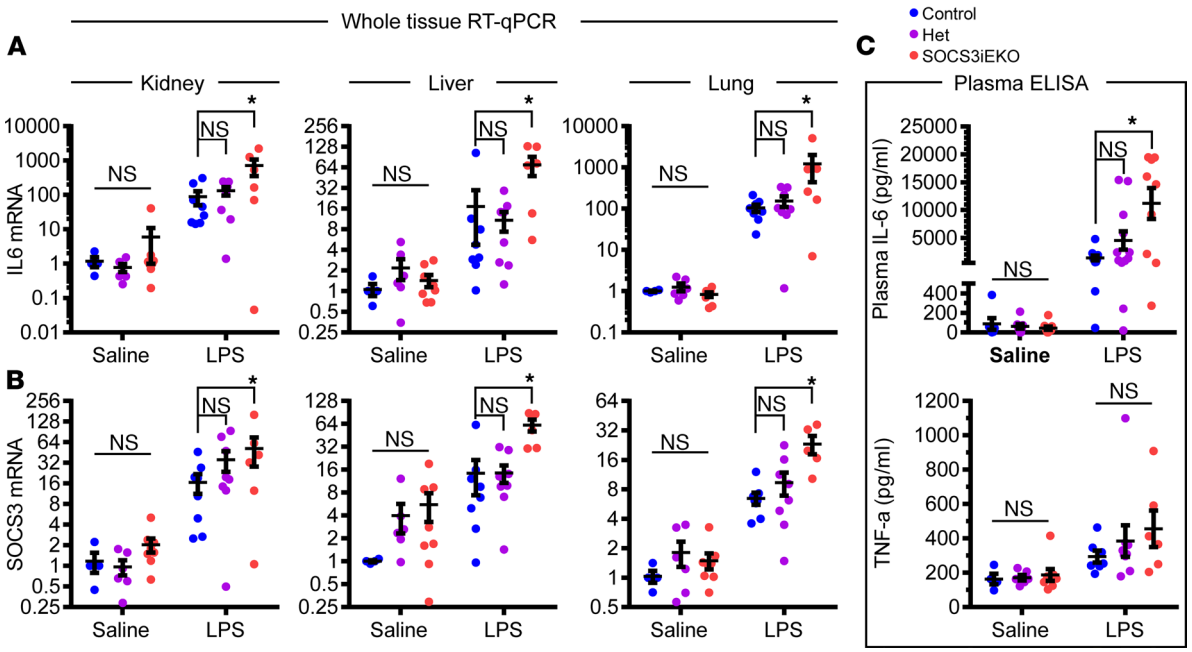

Figure 2. Overactivation of the IL-6/STAT3/SOCS3 pathway in endotoxemic SOCS3^{iEKO} mice. (**A**) Levels of IL-6 mRNA as measured by RT-qPCR obtained from whole organs. (n = 4–8.) (**B**) SOCS3 mRNA levels from the same sources. (**C**) Plasma levels of IL-6 and TNF-α as measured by ELISA. (n = 6–12.) All data in this figure were analyzed by 2-way ANOVA with Dunnett's post hoc test, comparing het or SOCS3^{iEKO} mice versus control. Asterisks denote $P < 0.05$. Data combined from at least 3 independent experiments.

While changes in lung and liver function are minor, our studies suggest that kidney failure is the main driver of endotoxin-induced mortality in SOCS3^{iEKO} mice. Blood urea nitrogen (BUN) levels were elevated in SOCS3^{iEKO} mice compared with control mice after endotoxin (Figure 4E). Contrary to this, creatinine levels were increased by LPS, but changes were not statistically significant between SOCS3^{iEKO} and control mice (Figure 4F). Direct measurement of glomerular filtration rate (GFR) showed that, consistent with previous reports (35–37), endotoxin in control mice induced a strong reduction in kidney function (Figure 4G). Deletion of SOCS3 from the endothelium induced a much more severe response, suggesting complete kidney failure, as seen by the fact that there was no clearance of FITC-sinistrin within the 90-minute period of this assay (Figure 4G).

In HUVECs, SOCS3's rapid degradation limits its inhibitory function on IL-6 signaling. Our findings not only showed that endothelial SOCS3 has a critical role to sustain organ function and promote survival after an endotoxin shock but also suggested that the regulation of SOCS3 levels critically affects its function. Thus, we set out to perform several in vitro studies to better understand how SOCS3 protein levels affected IL-6 signaling in endothelial cells. Previously, we have shown that HUVECs treated with a combination of recombinant IL-6 and sIL-6Rα (herein, IL-6+R) have a 30% loss in barrier function (26) that is sustained for at least 24 hours. To assess if sustained signaling downstream of IL-6 receptor activation was required to maintain the barrier function loss, we treated HUVECs with IL-6+R for 6 hours to allow for full barrier function loss prior to adding a blocking anti–IL-6 antibody or nonspecific IgG. As shown in Figure 5A, IL-6 inhibition completely reversed IL-6+R–induced increase in monolayer permeability. Similarly, addition of the JAK inhibitor ruxolitinib (rux) was sufficient to rescue the full barrier function in HUVECs even when added up to 24 hours after the IL-6+R challenge (Figure 5B). Consistent with a sustained IL-6+R signaling throughout this long period, we detected large increases in SOCS3 and IL-6 mRNA levels 24 hours and 48 hours after IL-6+R treatment (Figure 5C).

Given that SOCS3 remained elevated even as IL6+R caused a sustained barrier loss, we questioned whether SOCS3 has a protective, antiinflammatory function in HUVECs. To assess this, we decreased SOCS3 expression in HUVECs by utilizing 3 individual siRNA sequences, followed by treatment with IL-6+R. As shown in Figure 5D, SOCS3 knockdown led to a minor, albeit consistent, increase in IL-6+R–induced STAT3 phosphorylation at tyrosine 705, demonstrating that SOCS3 can act as a weak negative regulator of this pathway. Moreover, SOCS3 depletion further exacerbated the barrier function loss induced by IL-6+R without having any effect in the absence of IL-6+R (Figure 5E).

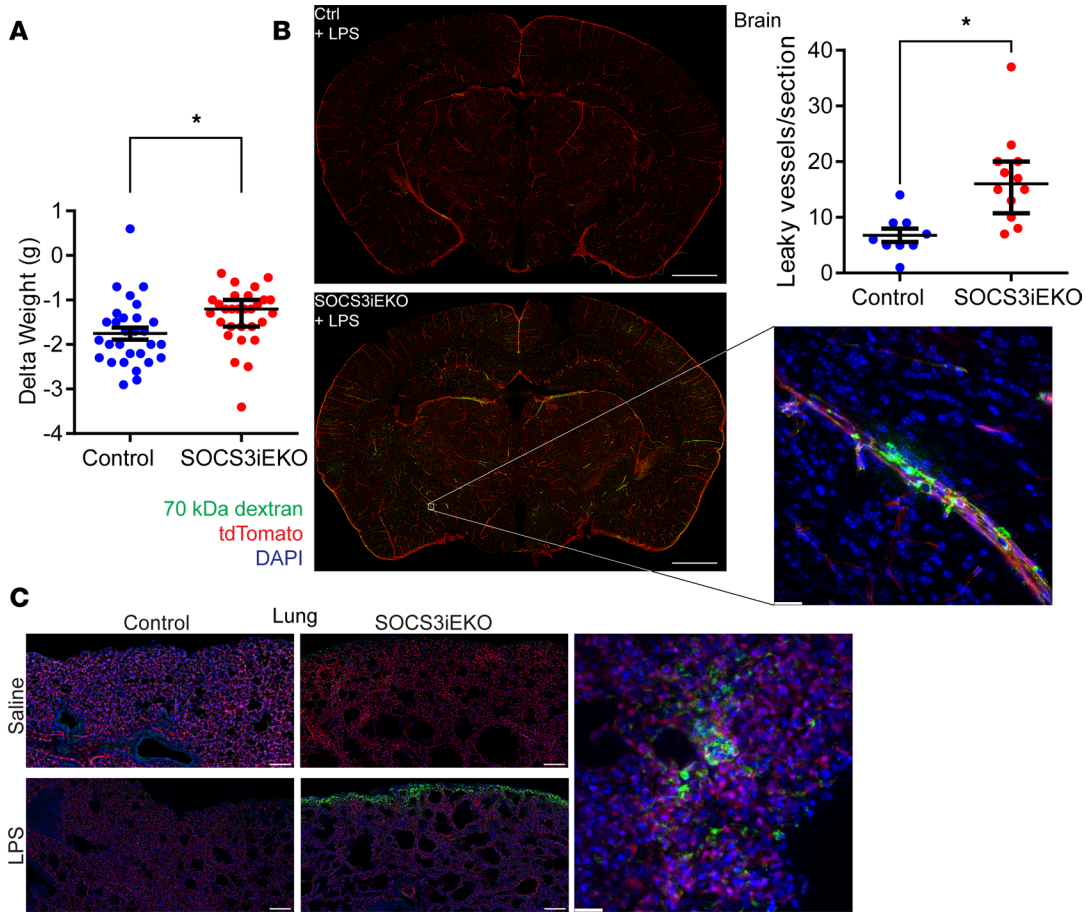

Figure 3. Increased vascular leakage in endotoxemic SOCS3^{iEKO} mice. (**A**) Weight difference before and 15–16 hours after LPS injection (Mann-Whitney, *n* = 20–29). (**B**) Brain sections of endotoxemic mice injected with FITC-labeled 70 kDa dextran. Shown on the left are full section images (bregma ~–2 mm, bar = 1 mm) and on the right a 63× original magnification of a cortical leaky vessel (maximum projection of a *Z*-stack covering near 100 μm, bar = 20 μm). Shown in the top right is the quantification of the number of cortical vessels per section (1 section per mouse, Mann-Whitney, *n* = 9-12). (**C**) Representative regions of 50 μm thick lung sections (left, bars = 100 μm) and a detail of a leaky spot near the lung edge (right, bar = 20 μm). Asterisks denote $P < 0.05$. Data combined from at least 3 independent experiments.

While the above data demonstrated that SOCS3 was able to reduce IL-6+R signaling, they also showed that this inhibition was not robust. Given that prior reports showed that SOCS3 has a short protein life span due to ubiquitin-mediated proteasomal degradation (38, 39), we hypothesized that fast ubiquitination and degradation would not allow for sufficient SOCS3 protein accumulation needed for a more robust inhibition of the pathway, despite the very high mRNA levels. To test this, we pretreated HUVECs with the proteasome inhibitor MG-132, followed by an IL-6+R challenge. MG-132 pretreatment effectively led to a robust increase in SOCS3 protein levels after IL-6+R treatment (Figure 6A). Importantly, the same protein lysates showed a strong inhibition of STAT3 phosphorylation 2 hours after challenge, suggesting that increased SOCS3 protein levels can act as a strong negative inhibitor of IL-6+R signaling (Figure 6A). We then determined the rate of turnover of SOCS3 by a cycloheximide-mediated (CHX-mediated) pulse and chase experiment. We treated cells with IL-6+R for 2 hours (to allow for SOCS3 expression), followed by the addition of CHX or PBS 2–30 minutes prior to lysing. SOCS3 protein expression was measured by Western blot. We found that SOCS3 turnover was extremely rapid in these cells, with a half-life between 10 and 20 minutes (Figure 6B).

We then sought to directly test the hypothesis that SOCS3 ubiquitination limited its function in HUVECs. We generated lentiviral vectors to overexpress tagged versions of either WT-SOCS3 or a degradation-resistant mutant (K6Q-SOCS3) (39). The SOCS3 construct was joined to turbo GFP (tGFP) via a P2A linker (40), thus allowing for expression of equimolar quantities of SOCS3 and free tGFP (Figure 6C). As expected, the mutation at lysine 6 led to higher accumulation of the exogenous SOCS3 protein even in the absence of IL-6+R (Figure 6D), which was associated with increased stability of this mutant (Figure 6E).

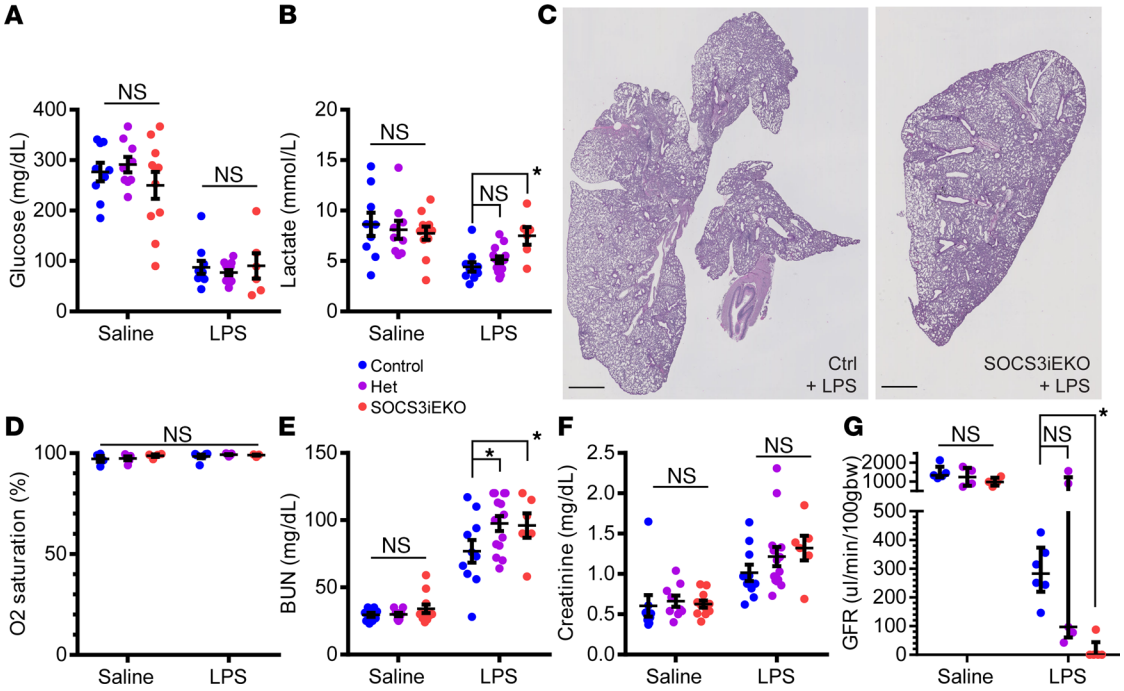

Figure 4. Mild lung injury and severe kidney failure in endotoxemic SOCS3^{iEKO} mice. (**A** and **B**) Endotoxin-induced hypoglycemia (**A**) and changes in circulating lactate (**B**). Two-way ANOVA and Holm-Šídák post hoc tests comparing het and SOCS3^{iEKO} mice with control within saline- or LPS-treated groups. (n = 6–14.) (**C**) H&E staining of 5 μm lung sections showing mild infiltration. (**D**) Normal blood O_2 saturation levels in all groups (2-way ANOVA). (**E** and **F**) Blood levels of urea nitrogen (**E**) and creatinine (**F**). Two-way ANOVA and Holm-Šídák post hoc tests comparing het and SOCS3^{iEKO} mice with control within saline- or LPS-treated groups. (**G**) Glomerular filtration rate measured for 90 minutes starting 14 hours postinjection of endotoxin or saline. Two-way ANOVA and Holm-Šídák post hoc tests comparing het and SOCS3^{iEKO} mice with control within saline- or LPS-treated groups. (n = 6–14.) Asterisks denote $P < 0.05$. Data combined from at least 3 independent experiments.

Moreover, overexpression of K6Q-SOCS3 led to a strong reduction of IL-6+R–induced STAT3 phosphorylation, whereas overexpression of WT-SOCS3 promoted a more modest reduction (Figure 6D). Consistently, exogenous WT-SOCS3 reduced IL-6+R–induced barrier function loss, while K6Q-SOCS3 overexpression prevented barrier loss altogether (Figure 6F).

IL-6 induced a proinflammatory gene expression profile in HUVECs involving a type I IFN–like response. We had previously shown that inhibition of de novo mRNA or protein synthesis prior to an IL-6+R challenge prevented the loss of barrier function (26). Because of the need for sustained signaling (Figure 5), we determined whether sustained protein synthesis was also required. CHX treatments up to 4 hours after IL-6+R challenge completely reversed the barrier function loss (Supplemental Figure 3A). Thus, we sought to determine the transcriptional changes that occurred during this time frame by performing an RNA-Seq analysis of cells treated or not for 3 hours with IL-6+R, in the presence or absence of rux. We identified 275 genes that were significantly (adjusted $P < 0.001$) induced (>2-fold) and 64 significantly repressed genes by IL-6+R. The top 50 most significant genes are shown in Figure 7A. Of note, JAK inhibition completely abolished the IL-6+R response (1 gene upregulated, 4 genes downregulated vs. DMSO). We performed RT-qPCR validation experiments on cells treated with IL-6+R for up to 24 hours, as well as on STAT3-knockdown cells treated with IL-6+R for 1 or 6 hours on over 30 genes of the top 100 induced gene set (Figure 7B, Supplemental Figure 3B, and data not shown). Bioinformatic analysis of these data using the ISMARA package (41) showed that this IL-6+R treatment induced the expected enrichment of STAT3-responsive genes but also a strong type I IFN–like response (Figure 7C). STRING (42) analysis showed a tight network of functional interactions linking multiple transcription factors of the STAT and interferon regulatory factor (IRF) families (Figure 7D). Consistently, IL-6+R promoted an increase in IFN-responsive genes that was abrogated by overexpression of SOCS3 (Figure 7E). This appears to be due to a direct effect of STAT3 rather than an indirect mechanism through IFN autocrine signaling, since IL-6+R or SOCS3 overexpression did not induce any significant change in the expression of type I IFNs (Supplemental Figure 3C) and the levels of IFN-α, IFN-β, and IFN-γ in the conditioned medium of IL-6+R–treated HUVECs remained below the level of detection as measured by ELISA (data not shown).

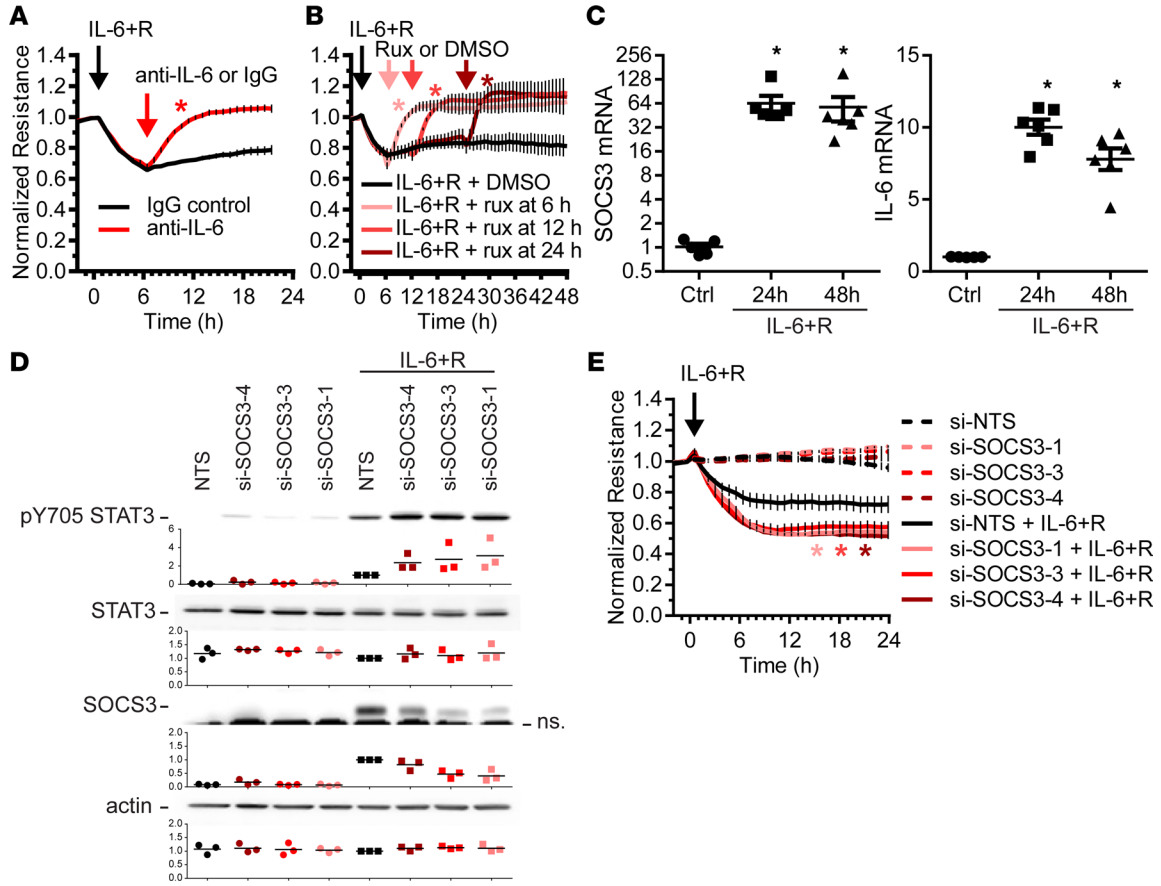

Figure 5. SOCS3 moderately reduces the effects of sustained IL-6 signaling in HUVECs. (**A** and **B**) HUVECs treated with a combination of recombinant IL-6 and sIL-6Rα displayed reduced barrier function that quickly recovered after antibody-mediated IL-6 blockade (**A**) or treatment with the JAK inhibitor rux (**B**). Two-way ANOVA of repeated measurements and Dunnett's post hoc tests comparing antibody (**A**) or rux (**B**) groups with the respective vehicle controls. (**C**) IL-6–induced transcriptional response is sustained for at least 48 hours (1-way ANOVA and Dunnett's post hoc test comparing IL-6+R–treated groups with control. (**D**) Western blot analysis showing a moderately increased level of STAT3 phosphorylation at tyrosine 705 in SOCS3 siRNA–treated cells compared with cells transfected with a nontargeting sequence (NTS). Levels of SOCS3 knockdown are shown above a nonspecific band (ns). pY705, phosphorylated tyrosine 705. (**E**) SOCS3 knockdown promotes a further loss of IL-6+R–induced barrier function loss but does not affect basal resistance levels. Two-way ANOVA of repeated measurements and Dunnett's post hoc tests comparing siSOCS3-transfected cells with NTS in the presence of IL-6+R. (n = 6.) Asterisks denote $P < 0.05$. Data representative of at least 3 independent experiments.

Endotoxin-induced transcriptional profiling in SOCS3^{iEKO} mice demonstrates a proadhesive, prothrombotic phenotype associated with a type I IFN–like response. To determine whether a similar transcriptional profile occurred in SOCS3^{iEKO} endotoxemic mice, mice were challenged for 15 hours with or without endotoxin prior to euthanasia followed by mRNA isolation from lungs, kidneys, and livers. We then assayed the expression of over 50 genes from each organ by RT-qPCR. De novo clustering of these data generated 3 distinct groups of mice (Figure 8A). Unsurprisingly, mice treated with saline solution clustered separately from those treated with LPS, with the exception of 1 LPS-treated heterozygous mouse that did not show any symptoms following the LPS injection. All other LPS-treated mice clustered in the 2 other groups: one included most control mice, while the other comprised mostly SOCS3^{iEKO} mice, demonstrating that the differences in the severity of the response closely correlated with their gene expression profile. Consistent with an intermediate response, both clusters contained several SOCS3-heterozygous mice. We then performed a principal component analysis (PCA) of all the data obtained from these mice, including the gene expression data and all physiological parameters (temperature, weight loss, blood counts, plasma IL-6 levels, creatinine, BUN, lactate, etc.). As shown in Figure 8B, all endotoxemic SOCS3^{iEKO} mice clustered separately from LPS-treated control mice, with most heterozygous again with intermediate changes. A functional assessment of each parameter in the first 2 PCA dimensions suggested that many transcriptional changes found in the kidneys drive a different phenotype than changes in either lungs or livers (Figure 8C). The severity score, BUN, creatinine, and plasma IL-6 effects, however, were more closely associated with lung and liver changes. To further investigate

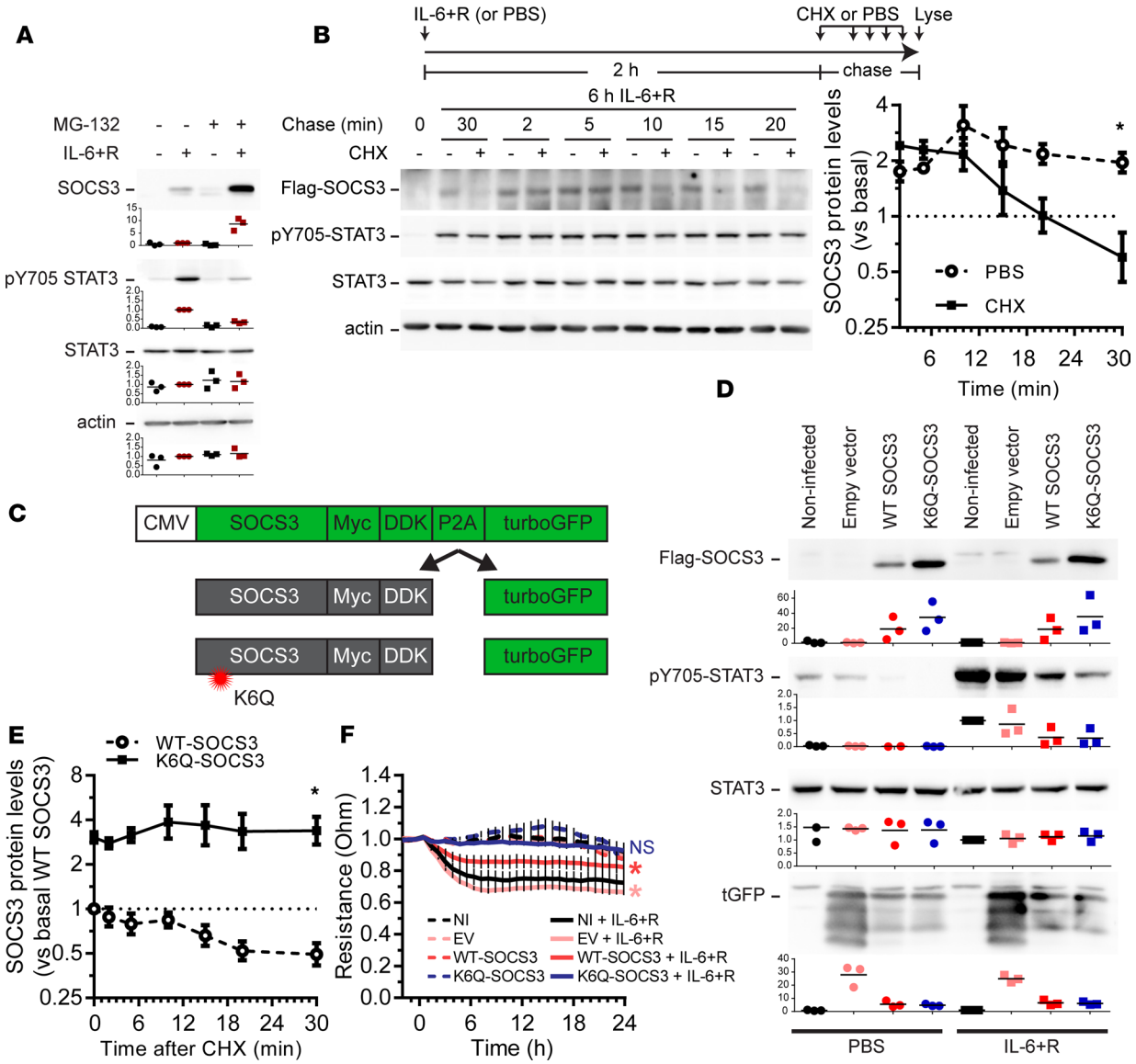

Figure 6. Levels of SOCS3 protein are rapidly degraded by the ubiquitin/proteasome pathway. (**A**) Western blot analysis showing SOCS3 expression and STAT3 phosphorylation levels 2 hours after treatment with IL-6+R in the presence or absence of the proteasome inhibitor MG-132. (**B**) Pulse-chase experiment of cells treated for 6 hours with IL-6+R and then for the specified time with either PBS or the protein synthesis inhibitor CHX prior to lysis. Representative Western blots (left) and quantification of 3 independent experiments (right). Two-way ANOVA with Dunnett's post hoc test (CHX vs. PBS). (**C**) Diagram of the SOCS3 overexpression strategy. (**D**) Western blots showing the expression levels of exogenous SOCS3 and their effects on IL-6+R–induced STAT3 phosphorylation. (**E**) Quantification of pulse-chase experiments by measuring the levels of Flag-SOCS3 after CHX. Two-way ANOVA with Dunnett's post hoc test (K6Q- vs. WT-SOCS3). (**F**) Transendothelial electric resistance measurements of monolayers expressing the different constructs and treated with either PBS or IL-6+R. Two-way ANOVA of repeated measurements with Dunnett's post hoc test (vs. PBS-treated, noninfected cells). Asterisks denote $P < 0.05$. Data representative of at least 3 independent experiments.

how gene expression changes were associated with pathophysiological parameters, we performed a complete cross-correlation analysis of all the data obtained from each endotoxemic mouse (Supplemental Figure 4A). We observed multiple clusters with close cross-correlation, including 2 large clusters that had a high correlation with the severity score (all significantly associated changes are shown in Supplemental Figure 4B). Notably, the levels of plasma IL-6 showed the highest correlation with the severity score, closely followed by BUN levels and the degree of temperature loss. The expression of lung PLAUR, liver ICAM, and kidney RHOU were the transcriptional changes with the highest correlation with the severity score and plasma IL-6 (Supplemental Figure 4B). Interestingly, RHOU was also dramatically increased by an IL-6+R treatment in HUVECs (Figure 7). Kidney injury markers, such as synaptopodin (SYNPO), also significantly correlated with the severity score, albeit with a much lower *R* value (Supplemental Figure 4C).

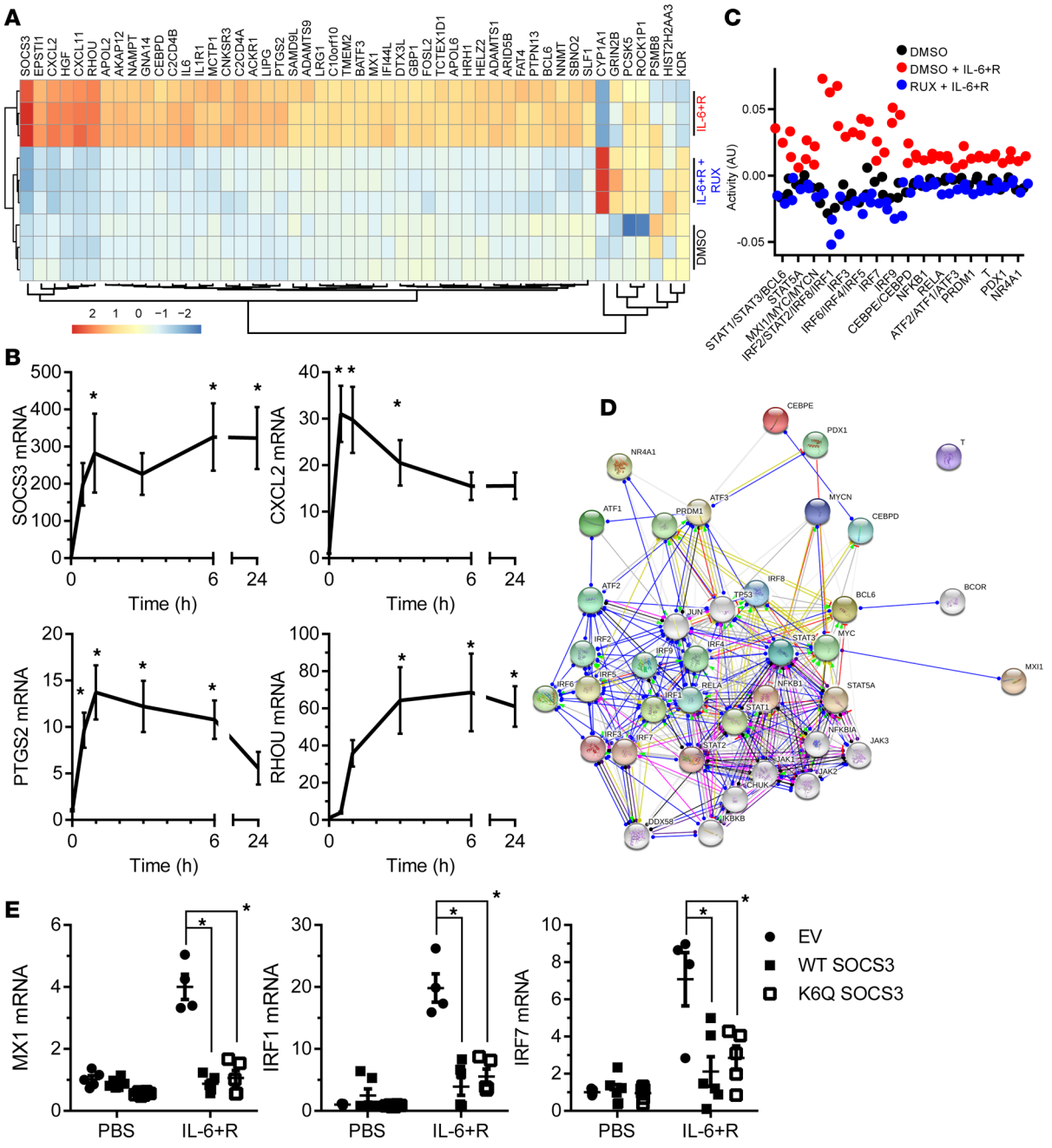

Figure 7. IL-6–induced gene expression profile in HUVECs. (**A**) Heatmap and unbiased clustering of cells treated with either PBS or IL-6+R after 30-minute incubation with either rux or DMSO (vehicle control). Ribosomal RNA–depleted RNA was assayed by RNA sequencing. Shown are the 50 most significant differences between IL-6+R and PBS, sorted by $\log_2$ fold change difference. One experiment performed in triplicate. (**B**) RT-qPCR analysis of an IL-6+R time course to confirm the changes in mRNA expression of selected candidate genes. One-way ANOVA and Dunnett's post hoc (vs. no IL-6+R, $n = 6$). Combined data from 3 independent experiments each performed in duplicate. (**C**) ISMARA of gene expression changes using the FASTQ files obtained in **A** showing a significant enrichment in type I interferon responses. (**D**) STRING representation of the main interconnections of genes identified in **C**. (**E**) RT-qPCR of cells treated with or without IL-6+R after infection with lentivirus to overexpress WT-SOCS3 or K6Q-SOCS3. An empty vector lentivirus was used as control. Two-way ANOVA and Dunnett's post hoc tests ($n = 4$–6). Combined data from 3 independent experiments each performed in duplicate. Asterisks denote $P < 0.05$. RHOU, ras homolog family member U; PTGS2, prostaglandin-endoperoxide synthase 2; MX1, MX dynamin like GTPase 1.

In agreement with a strong type I IFN–like response observed in IL-6+R–treated HUVECs, all organs examined showed a dramatic increase in many IFN-responsive genes (including MX1, IRF8, and OASL1) in endotoxemic mice, which was further aggravated by the loss of endothelial SOCS3 (Figure 9A and Supplemental Figure 5). This increased IFN-like transcriptional response was also associated with altered mRNA levels coding for leukocyte adhesion molecules and with a prothrombotic phenotype (Figure 9, B

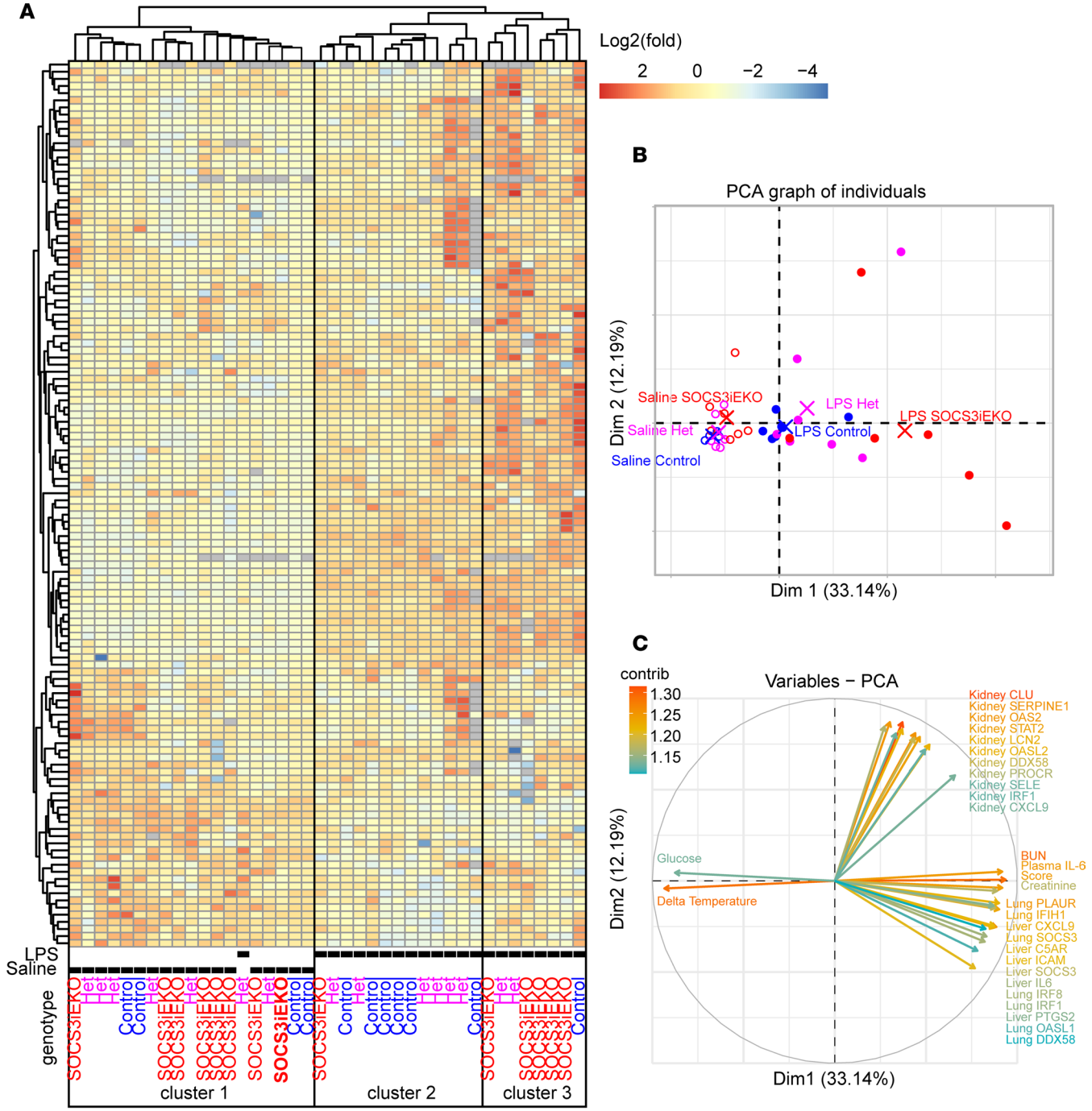

Figure 8. Loss of endothelial SOCS3 aggravates the transcriptional response to endotoxin in multiple organs. (**A**) Heatmap and unbiased clustering of mice 15–16 hours after injection of endotoxin based on gene expression changes as measured by RT-qPCR from whole-organ RNA (lungs, livers, and kidneys) and transformed through a base 2 logarithm. Data combined from 3 independent experiments (n = 4–8). (**B** and **C**) Principal component analysis of the raw expression data combined with all physiological parameters. Shown are the first 2 dimensions demonstrating a differential clustering of SOCS3^{iEKO} mice (**B**) and the main factors weighed in these 2 dimensions (**C**). Log_2 gene expression data are available as Supplemental Table 6 and all data including physiological parameters as Supplemental Table 7.

and C, and Supplemental Figure 5). Notably, P selectin expression was increased nearly 100-fold in the kidneys of endotoxemic SOCS3^{iEKO} mice. Similarly, tissue factor expression (coded by the F3 gene) increased only 2-fold in control mice but over 16-fold in SOCS3^{iEKO} mice, suggesting a severe dysregulation of the leukocyte adhesive and thrombomodulatory capacity of the endothelium of these knockout mice (Figure 9C). Immunofluorescence staining supported the increased expression of P selectin in every organ assessed

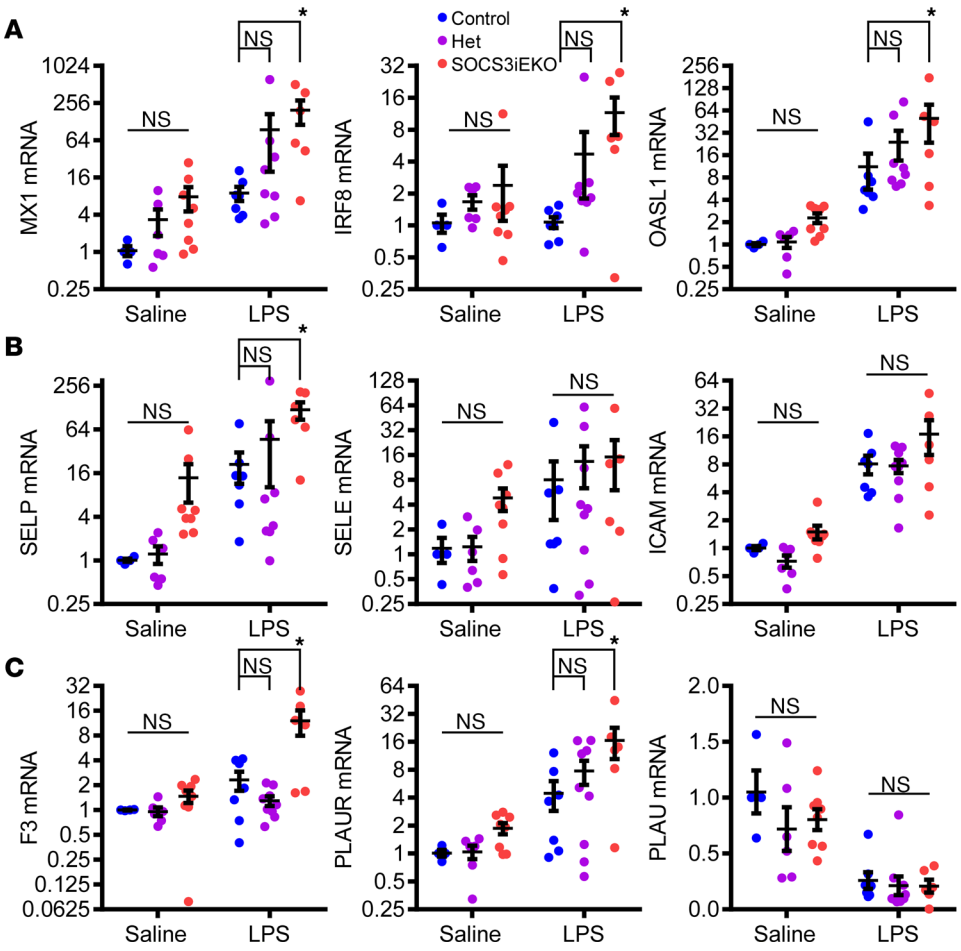

Figure 9. Transcriptional changes in whole kidneys of mice treated with endotoxin in the presence or absence of endothelial SOCS3. Loss of SOCS3 promotes a type I IFN–like response (**A**), as well as adhesive (**B**) and prothrombotic (**C**) changes after endotoxin. Two-way ANOVA and Holm-Šídák post hoc tests comparing het and SOCS3^{iEKO} mice with control within saline- or LPS-treated groups (n = 4–8). Data combined from 3 independent experiments. Asterisks denote $P < 0.05$. PLAUR, plasminogen activator, urokinase receptor.

of endotoxemic SOCS3^{iEKO} mice (Figure 10). Moreover, in these mice, P selectin was exposed on the luminal surface of the endothelium and not stored in Weibel-Palade bodies, suggesting that the transcriptional changes indeed led to an increased adhesivity to leukocytes of the affected vasculature.

Consistent with these findings, we observed accumulation of intravascular leukocytes in multiple tissues. We identified a large number of leukocytes adhered to the vessels of kidneys and lungs, as determined by H&E staining of FFPE sections (Figure 11A). Flow cytometry analysis of lungs showed a >2-fold increase in neutrophils upon treatment with LPS regardless of genotype (Supplemental Figure 6A). Consistent with the low levels of tdTomato$^+$ cells in blood and bone marrow (Figure 1), few Ly6G$^+$ cells were positive for tdTomato in lungs (Supplemental Figure 6A). Histochemical staining of FFPE sections for myeloperoxidase or F4/80 showed that both neutrophils and monocytes accumulated within the vessel lumens in lungs and kidneys (Supplemental Figure 6B). To better interrogate the extent of this intravascular accumulation, we obtained flat mounts of the retinas from these mice, which allowed us to study the whole-tissue vasculature. Staining with an anti-CD45 (pan-leukocyte) antibody demonstrated a dramatic accumulation of intravascular leukocytes (tdTomato$^-$CD45$^+$) that, in most cases, filled all retinal venules and colocalized with E selectin expression within the vessel lumens (Figure 11B). This accumulation was not evident on retinal arterioles or capillaries, further suggesting that this is due to increased adhesion to venules and not simply due to increased circulation of leukocytes within the retinal vasculature.

Increased neutrophil extracellular trap–osis is associated with organ injury in SOCS3^{iEKO} mice. Intravascular neutrophil extracellular traps (NETs) are commonly associated with increased tissue damage and vascular

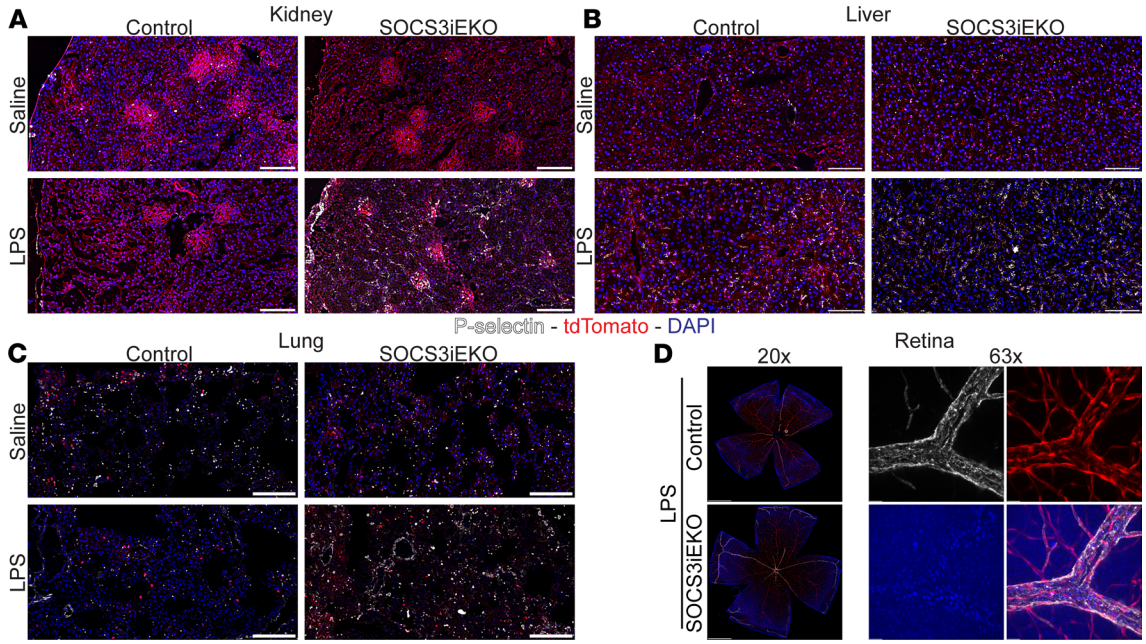

Figure 10. Loss of SOCS3 promotes an increase in P selectin expression after endotoxin. (**A**–**C**) Representative images of thin sections of kidney (**A**), liver (**B**), and lung (**C**) stained with anti–P selectin (white) and DAPI (blue). tdTomato expression is shown in red. (**D**) Whole-retina flat mounts (left) and a detail of a vein shown as a maximum projection of a *Z*-stack. Bars = 100 μm (**A**–**C**), 500 μm (**D**, left), or 20 μm (**D**, right). Representative images of 3 independent experiments.

dysfunction (43, 44). Thus, we next questioned whether loss of endothelial SOCS3 may lead to increased NETosis upon LPS exposure, by staining frozen sections for citrullinated histone H3. As shown in Figure 11C, LPS-induced increase in kidney NET formation in control mice was largely augmented in SOCS3^{iEKO} mice, supporting the notion that the accumulated intravascular leukocytes may have a causal effect in promoting tissue injury. NETs were found within the glomeruli and surrounding convoluted tubules. We observed a similar increase in NETosis in SOCS3^{iEKO} livers. Quantification of liver and kidney NETosis is presented in Figure 11D. Increased leukocyte adhesion, thrombosis, and NET formation may lead to reduced kidney perfusion, explaining the observed lack of kidney function in endotoxemic SOCS3^{iEKO} mice. Kidneys from these mice showed a dramatically reduced accumulation of 70 kDa FITC-dextran within the convoluted tubules 30 minutes after inoculation, with many regions lacking any fluorescence (Figure 11, E and F), suggesting lack of perfusion in these areas.

Discussion

Here, we present evidence to support the notion that endothelial SOCS3 is a crucial limiting factor for IL-6 signaling, promoting vascular homeostasis and survival during critical illness. An amplified JAK/STAT3 signaling in the endothelium caused severe vasculopathy, including a proinflammatory transcriptional profile leading to increased adhesivity and thrombogenicity of the endothelial surface, that was associated with a strong type I IFN–like response. This, in turn, led to leukocyte accumulation within the affected vascular lumens, NETosis, and kidney failure. Mechanistically, the exact levels of SOCS3 were maintained by a balance between a large transcriptional increase and very fast protein degradation via ubiquitination of lysine 6 and proteasomal degradation. Overall, the findings of this study reinforce the critical role of the endothelium in acute systemic inflammation and point to a pivotal role for SOCS3 stabilization as a therapeutic target.

An overactivated endothelium is key in the body's unmanaged response during inflammation, MODS (3–6, 45, 46), and recently, COVID-19 (47, 48). Thus, there is an urgent need to understand critical signaling pathways that influence the endothelium to respond in this manner. Our research focused on a signaling mechanism that we hypothesized may act as the tipping point between a beneficial immune response and an uncontrolled response that increases the risk of death or long-term sequelae. The circulating levels of IL-6 are not only closely associated with APACHE II and SOFA scores in septic patients but also very valuable as a prognostic marker of shock mortality (8–14). The murine model here used a single endotoxin injection to induce a severe systemic inflammatory reaction that was not lethal in control mice but led to

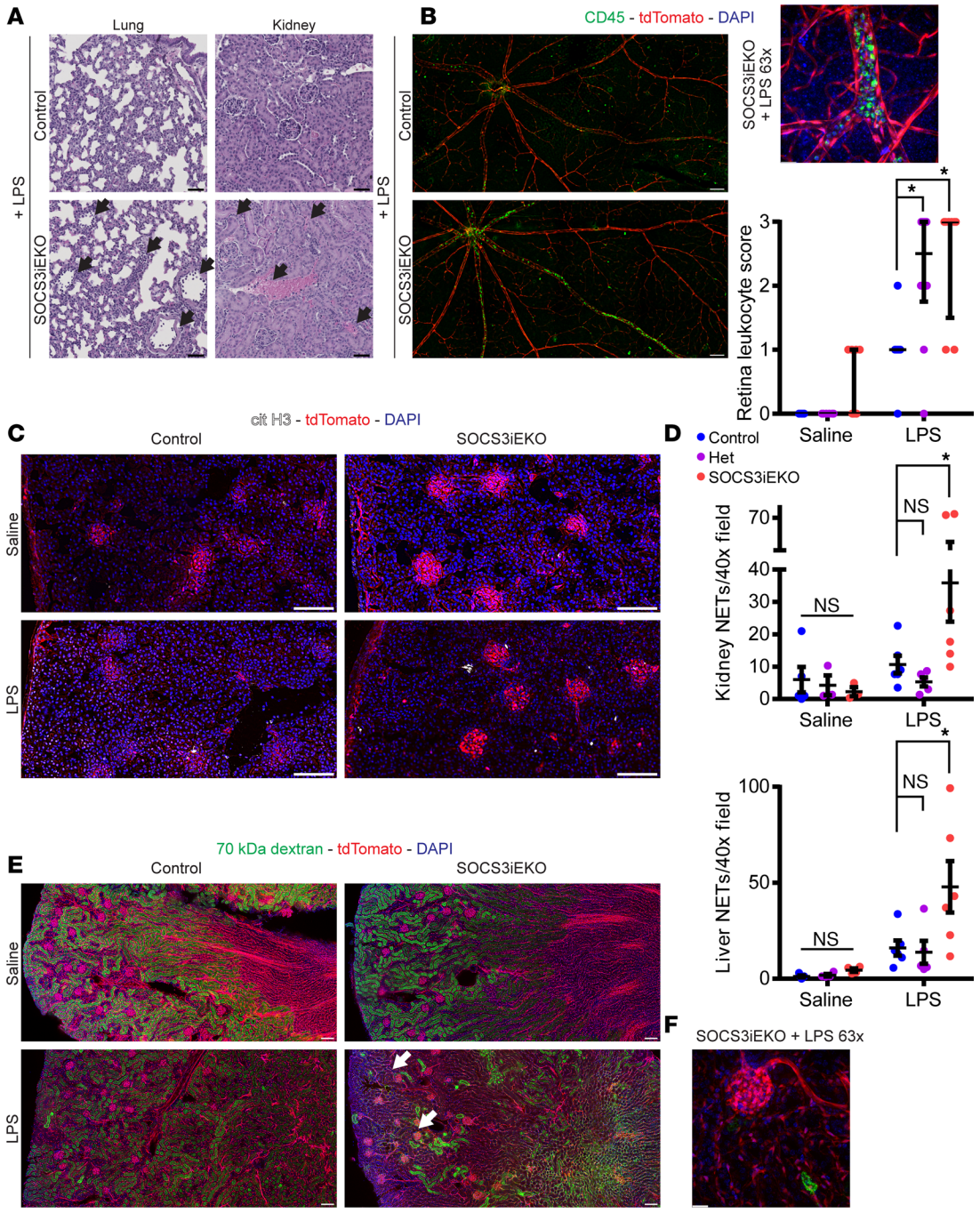

Figure 11. Increased intraluminal leukocyte accumulation and NETosis in endotoxemic SOCS3^{iEKO} mice. (**A**) Representative H&E images of thin FFPE sections of lungs and kidneys of LPS-treated control or SOCS3^{iEKO} mice. Arrows point to regions of leukocytes adhered to the vessel walls. (**B**) Whole-retina flat mounts were stained with CD45 (green) and counterstained with DAPI (blue). tdTomato is shown in red. Left, original magnification 20× tiled images (bar = 100 μm). Top right, detail of a vein showing dramatic leukocyte accumulation (bar = 20 μm). Lower right, scoring of 3 independent experiments (0: No intravascular CD45$^+$ cells. 1: Occasional, <10 in total, CD45$^+$ cells. 2: Multiple cells in >1 vein, occasional small clump. 3: >3 veins compromised, several clumps > 10 cells). Two-way ANOVA and Dunnett's post hoc tests comparing het and SOCS3^{iEKO} mice with control within saline- or LPS-treated groups. (n = 5–10.) Asterisks denote $P < 0.05$. (**C**) Representative images of 5 μm kidney sections stained with an antibody against citrullinated histone H3 (cit H3). Blue, DAPI; red, tdTomato (bar = 100 μm). (**D**) Quantification of data from 5 μm kidney and liver sections from 3 independent experiments. Mann-Whitney test (n = 3–6). (**E**) Representative images of thick (50 μm) kidney sections from mice injected with FITC-labeled 70 kDa dextran showing a reduction of green fluorescence intensity in control LPS mice and regions with convoluted tubules devoid of fluorescence in endotoxemic SOCS3^{iEKO} mice (white arrow). (**F**) A detail of a glomerulus and surrounding tubules lacking any dextran in endotoxemic SOCS3^{iEKO} mice (bar = 20 μm). Representative images of 3 independent experiments.

MODS in mice lacking SOCS3 in the endothelium, at least in part through vascular dysfunction including thrombosis, leukoembolization, and intravascular NETosis. These defects, in turn, resulted in systemic vascular leakage, organ hypoperfusion, and ultimately organ failure and death, thus closely mimicking the disease progression of critically ill patients (3–5).

Current published data argue for both pro- and antiinflammatory activities of endothelial STAT3. An increase in endothelial STAT3 phosphorylation is commonly associated with the inflammatory response (49–57). For example, LPS promotes a rapid increase in endothelial STAT3 phosphorylation (54–57) and the expression of IL-6Rα (58) and JAK3 (59). Confirming a critical role for this pathway in the inflammatory response, JAK or STAT3 pharmacological inhibitors improved survival of septic mice and rats (60–63), and a JAK inhibitor reduced ICAM-1 expression and vascular leakage in myocardial endothelium of LPS-injected mice (64). In contrast, disruption of STAT3 in the endothelium and hematopoietic cells using a Tie2-Cre transgene driving $STAT3^{fl/fl}$ excision led to a marked intestinal infiltration after an LPS challenge (65), lack of dendritic cell development (66), and increased myocardial apoptosis after ischemia/reperfusion injury (67). Using a similar approach with a Tie2e-Cre driver that shows increased endothelial specificity (68), it was shown that endothelial STAT3 ablation leads to increased susceptibility to LPS (68), hyperoxia-induced lung injury (69), and hepatic inflammation after ethanol ingestion (70). These findings demonstrate unequivocally that STAT3 expression is critical to sustain endothelial function but contradict the pharmacological data discussed above. Thus, we sought to determine the effect of STAT3 overactivation in the context of systemic inflammation. To achieve that, we took advantage of the negative regulation through expression of SOCS3 (9, 17). SOCS3 is integral to survival, since homozygous germline deletion of SOCS3 leads to embryonic lethality between days E11 and E13, mainly due to placental defects (71). Further, removal of SOCS3 from varying cell types using various tissue-specific Cre drivers demonstrated important, nonredundant roles in hepatocytes, myeloid cells, all hematopoietic cells, and others through increased signaling in response to inflammatory mediators and other stimuli (72), further suggesting that STAT3 overactivation has deleterious effects. Here, we show that removal of SOCS3 from the adult endothelium creates a primed endothelium that is more reactive to a proinflammatory insult. Moreover, our in vitro data suggest that inhibition of endothelial SOCS3 degradation is a promising avenue to prevent and/or revert vasculopathy during shock.

The data from this study indicate that removal of endothelial SOCS3 may indeed be one of the contributors to critical illness, at least in part by promoting an IL-6 amplifier mechanism, similar to that previously linked to worse prognosis (9). We noted that endotoxin-treated $SOCS3^{iEKO}$ mice became extremely hypothermic, and this physiological change was statistically linked to the severity score and progression of inflammation. When comparing blood panels of these mice, versus their control counterparts, we were surprised to see that the levels of circulating leukocytes and platelets were not different between the groups. Histochemical, functional, and transcriptomic analyses demonstrate that loss of SOCS3 led to systemic alterations in multiple organs. Histological assessment showed modestly increased numbers of leukocytes in the lung interstitium, but not a gross increase in edema, suggesting that lymphatic draining was sufficient to balance the increased vascular permeability we observed in the fluorescent dextran experiments. Given the lack of overt histological changes in lungs and normal blood oxygen levels, it is clear that the intraluminal accumulation per se was not sufficient to induce tissue damage. This finding is consistent with the normal O_2 saturation we measured even in severely compromised mice, demonstrating that the lethality seen in endotoxemic $SOCS3^{iEKO}$ mice was not due to respiratory distress. Similar findings were previously reported in a model of cecal ligation and puncture (73). Similarly, we observed a loss of glycogen but no overt histological changes in liver sections. This finding, together with similar plasma albumin in all experimental groups, suggest that liver function was mostly maintained. Again, it has been previously shown that sepsis does not induce severe liver dysfunction (37), but instead, acute kidney injury. In fact, $SOCS3^{iEKO}$ mice showed severe kidney failure in response to LPS, as determined by direct GFR assays and confirmed by increased BUN levels, altered expression of kidney injury markers, and increased NETosis; increased NET formation has been previously associated with kidney dysfunction (74). How NETs form in this situation remains to be determined. Given the low amount of tdTomato-positive circulating cells (arguing against a direct effect of SOCS3 loss in neutrophils), we propose that signals derived from the endothelium (either soluble or through cell-cell contacts) are the most likely cause. Surprisingly, we also found massive leukoembolization in retinal venules and increased vascular permeability in large vessels irrigating the brain cortex. Although the blood-brain barrier is tightly regulated, it is often compromised in such disease states as Parkinson's, Alzheimer's, and acute inflammation (75). Importantly, many critically ill patients exhibit mental confusion and delirium (76–78), which is suggested to be due to impaired microvascular

perfusion (79). Moreover, intensive care unit survivors have increased risk of long-term cognitive impairment, which is correlated with the severity of acute illness (80). Although the fast lethality in this model did not allow for any assessment of cognitive function in these mice, this finding suggests a potential mechanism that would explain short-term and long-term cognitive dysfunction via localized edemagenic events driving brain damage.

Tissue perfusion in septic patients is drastically reduced, and microvascular changes are independent predictors of sepsis mortality (81–83). Many of our findings suggest that localized hypoperfusion was a main driver of lethality in the knockout mice. Lactate measurements after endotoxin in control mice were surprisingly lower than baseline levels. We hypothesized that this could be explained by the severe hypoglycemia induced by the endotoxin shock. However, SOCS3^{iEKO} mice showed much increased lactate levels compared with control mice, even if plasma glucose levels remained similarly low. This may suggest that there may be regions with increased hypoxic conditions. Consistent with this finding, we found that fluorescent dextran was unable to reach many regions of the kidney cortex in endotoxemic SOCS3^{iEKO} mice, demonstrating that, at least in the most severely affected organ, tissue hypoperfusion and thus localized hypoxia are features of this model. We did not observe a lack of perfusion of either lungs or livers, consistent with their increased function.

In our studies, we detected dramatically increased leukocyte adhesion in endotoxemic SOCS3^{iEKO} mice as measured by mRNA and protein levels of leukocyte receptors, as well as direct binding of leukocytes, including neutrophils and monocytes, to the vessel lumens. This increase is similar to that observed in septic patients (7, 84, 85). This was particularly evident in the retinal bed vasculature, where we detected increased E and P selectin levels, as well as dramatic leukoembolization throughout the venular system. Little is known about the involvement of the retinal microvasculature during shock. Notably, one study demonstrated a high incidence of retinal angiopathies in septic patients (86). Whether similar leukoembolization occurs in critically ill patients remains to be determined. In addition to this increase, SOCS3^{iEKO} mice had higher levels of prothrombotic factors over those seen in the endotoxic control mouse. In fact, tissue factor (F3) mRNA was greatly increased, notably in the kidney. This, along with reduced amounts of PLAU mRNA, led us to hypothesize that an increase in clotting may further aggravate the kidney hypoperfusion. We also detected increased levels of PLAUR expression. Although we do not know the source(s) or function of this change, it is consistent with clinical findings that demonstrate that circulating soluble uPAR levels are associated with systemic inflammation severity (87) and produced by neutrophils (88). The hypothesis that intraluminal neutrophils in endotoxemic SOCS3^{iEKO} mice may drive a hypercoagulatory state in this model remains, however, to be tested.

In vitro studies using HUVECs showed that IL-6 signaling led to a strong type I IFN–like response. Notably, we found that loss of endothelial SOCS3 greatly increased the expression of multiple IFN-responsive genes in all organs tested. Moreover, the expression of many of these genes was increased 2- to 4-fold in SOCS3^{iEKO} mice even in the absence of an endotoxin challenge. Conversely, a prior report showed that constitutive expression of type I IFNs sustains expression of JAKs and STATs and predisposes cells to necroptotic death (89). In turn, necroptotic pathways may lead to NETosis (90), another feature of this model. The similarities observed between our in vitro experiments in IL-6+R–treated HUVECs and SOCS3^{iEKO} mice strongly support the argument that the described phenotype corresponds to an activation of the observed IL-6 amplifier loop. However, SOCS3 can block other gp130-mediated signals, and thus it remains possible that other gp130 receptor family ligands are involved in this response; further studies (e.g., using IL-6 inhibiting antibodies) will be required to assess this possibility.

In summary, we demonstrate that endothelial SOCS3 promotes vascular homeostasis and survival in a murine model of endotoxemia. Loss of SOCS3 in the adult endothelium leads to severe vasculopathy and kidney failure under systemic inflammation that is associated with an increased type I IFN–like transcriptional program. Importantly, loss of a single allele induced an intermediate phenotype, suggesting that maintenance of high SOCS3 levels is an absolute requirement. In vitro experiments showed that endothelial SOCS3 is a highly unstable protein, due to ubiquitin-dependent proteasomal degradation. Thus, inhibition of endothelial SOCS3 degradation is a promising therapeutic opportunity to alleviate the vascular dysfunction during shock, increasing survival rates and reducing the risk of long-term sequelae.

Methods

Materials

The commercial sources for critical reagents and their catalog numbers are listed in Supplemental Table 1. Supplemental Table 2 lists all antibodies used. Supplemental Table 3 provides a list of sequences for RT-qPCR primers.

Mice

Genetics. Endothelial specific, tamoxifen-inducible SOCS3-knockout mice were generated by breeding B6.Tg(Cdh5-cre/ERT2)1Rha (Cdh5-CreER^{T2} endothelial driver) mice (91) (a gift from Kevin Pumiglia, Albany Medical College, Albany, New York, USA) with B6.Gt(ROSA)26Sor$^{tm9(CAG-tdTomato)Hze}$ (ROSA26-tdTomato reporter) (92) and B6;129S4-Socs3^{tm1Ayos}/J (SOCS3$^{fl/fl}$ conditional knockout) (93) mice (The Jackson Laboratory). Mice were backcrossed to a full C57BL6/J background by breeding to C57BL6/J mice (The Jackson Laboratory) for at least 10 generations. Knockouts and heterozygous and control littermates were obtained by crossing Cre^{+} tdTomato^{+} SOCS3$^{fl/+}$ mice. Genotypes and sex were confirmed by PCR genotyping (Supplemental Table 4). All mice received tamoxifen (2 mg tamoxifen in 100 μL via intraperitoneal [IP] injection) at 6–9 weeks old for 5 consecutive days. Deletion of the target gene after tamoxifen was confirmed by tail digestion and PCR. All the experiments were conducted between 2 and 3 weeks after the end of tamoxifen treatment.

Housing. Mice were housed in specific pathogen–free rooms with 12-hour light/12-hour dark cycle and controlled temperature and humidity. Mice were kept in groups of 5 or fewer in Allentown cages with access to food and water ad libitum.

Endotoxemic model. Severe, acute inflammation was induced by a single IP injection of a bolus of 250 μg/250 μL LPS. Control mice were given 250 μL of sterile saline via IP injection. A severity scoring system was used to assess the response to LPS based on recently described scoring systems for similar conditions (32–34) (Supplemental Table 5). Body weight and temperature were obtained prior to LPS or saline injection and immediately after scoring.

Experimental design. Mice from at least 1 litter were used in each experiment. Mice from a second litter were used in some experiments to balance the number of mice for each sex in each experimental group. No mice were excluded from the studies. Assignment to the saline or LPS groups was performed through randomization of mice within each genotype for every litter. All handling, measurements, and scoring were performed blinded to treatment and genotype groups and based on mouse ID (ear tags). At least 3 independent experiments (from 3 or more litters) were performed for each assay. Experimental groups were unmasked at the end of each experiment.

Blood measurements

Blood for complete blood count was attained via a 5 mm lancet applied to the submandibular vein. Blood was collected into an EDTA blood collection tube and run on a Heska Element HT5 instrument. The remaining blood was centrifuged (1200*g*, 15 minutes, room temperature [RT]). Plasma was removed and stored at –80°C until further processing.

To collect blood for the chemistry panel, the inferior vena cava was snipped after pentobarbital administration, and blood was collected into capillary tubes connected to a lithium heparin-coated blood collection tube. Approximately 100 μL was loaded into an Element point-of-care (POC) card and run on a Heska Element POC Blood Gas and Electrolyte Analyzer.

Circulating levels of IL-6 and TNF-α were measured from plasma by ELISA following manufacturer's instructions, and plates were read on a Molecular Devices Spectramax I3. Circulating albumin from plasma was measured using the bromocresol purple method following the manufacturer's instructions. In addition to the supplied standards, mouse serum albumin was used as reference.

Glomerular filtration rate

GFR was measured as previously described (94). Briefly, 1 to 2 days prior to experiments, a small area of dorsal fur was removed using an electric shaver followed by application of depilatory cream. Approximately 14–15 hours post LPS or saline injection, mice were briefly anesthetized (3.5% v/v isoflurane) and placed on a heated pad at 37°C. A MediBeacon transdermal Mini GFR Monitor was attached to the depilated region using a double-sided adhesive patch and adhesive medical tape. The unit gathered a baseline measurement for approximately 1–2 minutes prior to injection of FITC-Sinistrin (MediBeacon) (7 mg/100 g BW) in sterile saline solution via retro-orbital injection. Upon recovery from anesthesia, each mouse was returned to its own cage without access to food and water. After 90 minutes the instrument was removed, and GFR was calculated with MediBeacon's proprietary software.

Assessment of vascular leak

Approximately 14–15 hours after LPS or saline injection, mice were briefly anesthetized (3.5% v/v isoflurane) and placed on a heated pad at 37°C. Then, mice received 100 μL of saline containing 2 mg/mL of FITC-labeled

70 kDa dextran, and 0.13 mg/mL Alexa Fluor 647–labeled 10 kDa dextran was injected via retro-orbital injection. Upon recovery from anesthesia, mice were returned to the cages. After 30 minutes, mice were injected with pentobarbital. After confirmation of lack of paw reflex, the chest cavity was opened, and mice were perfused for 3 minutes with 5 mL/min RT PBS. Livers, kidneys, lungs, and brains were fixed in 10% neutral buffered formalin (NBF) for 24–48 hours. Fresh NBF was replaced 24 hours after organ collection. Then, kidneys, livers, and lungs were maintained at 4°C for 2 days or until organs sank in 15% sucrose and 30% sucrose (both in PBS with 0.1 g/L sodium azide), respectively, before embedding and freezing in Tissue-Tek optimal cutting temperature (O.C.T.). Frozen 50 μm sections on charged coverslips were stored at –20°C until needed. Brains were transferred directly to 30% sucrose, 0.1 g/L sodium azide in PBS at 4°C, until the organs sank (approximately 48 hours). Brains were embedded and frozen in O.C.T. prior to sectioning. Sections, 100 μm, were stored in 30% sucrose, 1% polyvinyl-pyrrolidone (average MW 40 kDa), 30% ethylene glycol, and 0.1 g/L sodium azide in PBS at 4°C until use. After mounting, images were taken at original magnification 20× and 63× using a Leica Thunder microscope and processed for computational clearing. Three-dimensional original magnification 63× stacks were processed with Imaris software (Bitplane). Vascular leak was observed as patches of green fluorescence outside the vessel lumens.

Histology and immunofluorescence

Histochemistry. Lungs, livers, and kidneys were collected and placed into 10% NBF and stored in 70% ethanol prior to embedding in paraffin. Sections, 5 μm, were then stained with Harris H&E following manufacturer's protocols. Slides were scanned at original magnification 40× on a Nanozoomer (Hammamatsu C10730-12).

Frozen tissue immunofluorescence. Harvested tissue was embedded in O.C.T. and snap-frozen in a dry ice and methanol slurry. Blocks were stored at –80°C until processed. Sections, 5 μm, were postfixed in 4% paraformaldehyde (PFA) for 15 minutes. After 3 washes in PBS, slides were permeabilized in PBS + 0.1% Triton X-100 (PBS-TX) for 15 minutes. Then tissue was blocked in 5% FBS in PBS-TX for 1 hour. Slides were stained with primary antibodies in blocking buffer overnight at 4°C or 2 hours at RT. Slides were then washed in PBS-TX and stained with Alexa Fluor–conjugated secondary antibodies and 0.5 μg/mL DAPI for 1 hour at RT. Slides were then washed in PBS and mounted with Fluoroshield. Images were taken at original magnification 20× and 63× using a Leica Thunder microscope and processed for computational clearing.

Retina whole mount. After euthanasia, eyes were placed in 4% PFA at 4°C. After 24 hours, eyes were transferred to PBS and stored at 4°C until the retinas were removed. After removal of the cornea and lens, the edge of the retina was gently detached from the sclera. Four small cuts were made to the retina to allow flattening. Then, retinas were permeabilized and blocked by incubating for 1 hour at 37°C with 1% BSA, 5% FBS, and 0.5% Triton X-100 in PBS with gentle shaking. Retinas were then incubated with primary antibodies in permeabilization/blocking buffer overnight at 37°C with gentle shaking. Retinas were then washed (3 times) in PBS and incubated with Alexa Fluor–conjugated secondary antibodies (if required) and 1 μg/mL DAPI in PBS at 37°C for 4 hours. Retinas were then washed (3 times) in PBS for 20 minutes/wash, flattened on the slides, and mounted with Fluoroshield. Images were taken at original magnification 20× and 63× using a Leica Thunder microscope and processed for computational clearing.

Cell culture and treatment

HUVECs were isolated in-house according to established protocols (27, 96–98). Briefly, umbilical cords (20–30 cm) from scheduled cesarean sections were stored at 4°C in PBS containing a mixture of penicillin and streptomycin and used within 24 hours. Samples were anonymized following the recommendations of the Albany Medical Center IRB. After quick rinses in 70% ethanol and sterile PBS, vein lumens were washed with PBS to remove remaining blood and clots and then incubated for 30 minutes at RT in sterile PBS containing 0.2% collagenase, pH 7.4, with gentle massaging. Released cells were collected in growth media containing phenol red–free EBM 2 media supplemented with EGM-2 Growth Medium 2 Supplement Mix, penicillin, streptomycin, and amphotericin B. Cells were then centrifuged at 300*g* for 10 minutes at room temperature, resuspended in fresh growth media, and plated in plastic culture flasks precoated with 0.1% gelatin. Upon reaching initial subconfluence (4–7 days), cells were passaged 3 times per week in the absence of antibiotics. Identity and purity of the HUVEC isolations were confirmed each time by more than 99% positive immunostaining with endothelial cell markers (FITC-*Ulex europaeus* lectin, VE-cadherin) and more than 99.9% negative for α–smooth muscle actin. Cells were assayed between passages 3 and 8. Unless otherwise stated, for all assays, cells were plated at full confluence at a density of 8×10^4 cells/cm^2 on plates precoated for 30 minutes with 0.1% gelatin and incubated at least 48 hours prior to the start of experiments.

HUVECs were treated with inhibitors to JAK activity (rux), proteasome (MG-132), or protein synthesis (CHX) dissolved in DMSO at a maximum use concentration of 0.1%. A similar amount of DMSO was added to vehicle control wells. To induce IL-6 signaling, cells were treated with a combination of 200 ng/mL recombinant human IL-6 and 100 ng/mL sIL-6Rα (IL-6+R).

Lentiviral delivery

We created lentiviral constructs to express SOCS3 with C-terminal Myc and DDK tags by subcloning the human SOCS3 coding sequence and tGFP in a single mRNA using a P2A linker following Origene's TrueORF cloning instructions. Briefly, SOCS3 cDNA was cut with EcoRI and XhoI and subcloned into pLenti-C-Myc-DDK-P2A-tGFP lentiviral gene expression vector. A lysine 6 mutation (K6Q-SOCS3) was obtained by PCR mutagenesis using PfuUltra II Fusion High-fidelity DNA Polymerase. All constructs were confirmed by Sanger sequencing (Genewiz).

Lentiviral particles were grown in HEK293FT cells (Invitrogen, Thermo Fisher Scientific, R700-07) by cotransfecting cells with the SOCS3-expressing lentiviral constructs or pLenti-C-Myc-DDK-P2A-tGFP (empty vector control) and pCMV-dR8.2 dvpr and pCMV-VSVG packaging plasmids (98). After 48 hours, medium was concentrated using a 30 kDa cutoff filter, aliquoted, and stored at –80°C until use. Viral titer was determined by the proportion of infected cells with green fluorescence 72 hours postinfection.

Measurement of monolayer permeability

Monolayer permeability was determined in real time by measuring changes in electrical resistance using Electrical Cell-Substrate Impedance Sensor (ECIS, Applied Biophysics). HUVECs were seeded onto 8- or 96-well electrode arrays precoated with 0.1% gelatin at confluence. Following treatments, the electrical impedance across the monolayer was measured at 1 V, 4000 Hz AC for 24–72 continuous hours every 5 minutes and then used to calculate electric resistance by the manufacturer's software.

RNA sequencing

Confluent HUVECs grown on 0.1% gelatin–precoated, 6-well plates were pretreated for 30 minutes with 2 μM rux or 0.1% DMSO control and then treated with IL-6+R or PBS for 3 hours in triplicate. RNA was isolated with TRIzol following manufacturer's instructions. RNA enrichment and next-generation sequencing were performed by Genewiz. Briefly, after RNA quality testing, rRNA was eliminated using a magnetic bead approach, and enriched RNA was subjected to fragmentation and random priming for cDNA synthesis. Following end repair, 5′ phosphorylation, and dA-tailing, adaptor ligation was performed using NEBNext adaptors. FASTQ files were obtained by collecting approximately 40×10^6 reads (2×150 paired end) per sample on an Illumina HiSeq instrument. The bioinformatics analysis was performed by following a workflow (99) using Salmon V0.8.1 (100), R/Bioconductor 3.5 (101), tximport (102), and DESeq2 (103). The data discussed in this publication have been deposited in NCBI's Gene Expression Omnibus (104) and are accessible through GEO Series accession number GSE163649 (https://www.ncbi.nlm.nih.gov/geo/query/acc.cgi?acc=GSE163649).

Statistics

All statistical analysis and graphs were made in GraphPad Prism version 6 or in R. Analysis for RNA and protein expression levels was performed using 1-way ANOVA and Dunnett's post hoc test or a 2-way ANOVA and Holm-Šídák post hoc tests comparing all samples versus a control (designated in each figure). Two-group comparisons were made with either 2-tailed Student's *t* test (for parametric data) or Mann-Whitney *U* tests for nonparametric data. A 2-tailed *P* value of less than 0.05 was considered significant. For Western blot experiments, normalized band intensity values (protein/actin) were used. ECIS data were analyzed by 2-way ANOVA of repeated measurements and post hoc analysis comparing main column (treatment) effects. All unsupervised clustering for heatmaps, PCAs, and cross-correlation studies was performed in R following a procedure described in the Supplemental Methods.

Study approval

Mice were housed at the Animal Research Facility at Albany Medical Center, a facility that has been accredited by Association for Assessment and Accreditation of Laboratory Animal Care International and licensed by the US Department of Agriculture and New York State Department of Health, Division of Laboratories and Research. All animal work was performed according to IACUC-approved protocols. Donors gave oral informed

consent for collecting HUVECs from deidentified discarded tissue. The requirement for written informed consent was waived by the Albany Medical Center Institutional Review Board. All HUVECs were stored in our cell bank, and no cord was obtained specifically for any single experiment.

Author contributions

NM and APA conceived and designed research; NM, RBR, SL, KL, LT, SS, and APA performed experiments; NM, RBR, SL, KL, LT, SS, GF, AJ, PAV, and APA analyzed data; NM and APA interpreted results of experiments; NM, RBR, SS, and APA prepared figures; NM drafted the manuscript; NM and APA edited and revised the manuscript with input from RBR, SL, KL, LT, SS, GF, AJ, and PAV; and NM, RBR, SL, KL, LT, SS, GF, AJ, PAV, and APA approved the final version of the manuscript.

Acknowledgments

This project was supported by the National Institute of General Medical Sciences/NIH grant R01GM124133 and an American Heart Association Transformational Project Award 18TPA34170561 to APA and National Heart, Lung and Blood Institute/NIH grants R01HL141127 and R01HL153019 to GF and K01-HL130704 to AJ. We are grateful to Joseph Balnis for his help in measuring O_2 saturation levels.

Address correspondence to: Alejandro P. Adam, Department of Molecular and Cellular Physiology, Albany Medical College, 43 New Scotland Avenue, Albany, New York 12208, USA. Phone: 518.262.9776; Email: adama1@amc.edu.

1. Kaukonen KM, et al. Systemic inflammatory response syndrome criteria in defining severe sepsis. *N Engl J Med*. 2015;372(17):1629–1638.
2. Tisoncik JR, et al. Into the eye of the cytokine storm. *Microbiol Mol Biol Rev*. 2012;76(1):16–32.
3. Ince C, et al. The endothelium in sepsis. *Shock*. 2016;45(3):259–270.
4. Feletou M, Vanhoutte PM. Endothelial dysfunction: a multifaceted disorder (The Wiggers Award Lecture). *Am J Physiol Heart Circ Physiol*. 2006;291(3):H985–1002.
5. van Ierssel SH, et al. The endothelium, a protagonist in the pathophysiology of critical illness: focus on cellular markers. *Biomed Res Int*. 2014;2014:985813.
6. Chang JC. Sepsis and septic shock: endothelial molecular pathogenesis associated with vascular microthrombotic disease. *Thromb J*. 2019;17(1):10.
7. Aird WC. The role of the endothelium in severe sepsis and multiple organ dysfunction syndrome. *Blood*. 2003;101(10):3765–3777.
8. Hunter CA, Jones SA. IL-6 as a keystone cytokine in health and disease. *Nat Immunol*. 2015;16(5):448–457.
9. Hirano T. Interleukin 6 in autoimmune and inflammatory diseases: a personal memoir. *Proc Jpn Acad Ser B Phys Biol Sci*. 2010;86(7):717–730.
10. Hou T, et al. Accuracy of serum interleukin (IL)-6 in sepsis diagnosis: a systematic review and meta-analysis. *Int J Clin Exp Med*. 2015;8(9):15238–15245.
11. Remick DG, et al. Role of interleukin-6 in mortality from and physiologic response to sepsis. *Infect Immun*. 2005;73(5):2751–2757.
12. Tanaka T, et al. IL-6 in inflammation, immunity, and disease. *Cold Spring Harb Perspect Biol*. 2014;6(10):a016295.
13. Biffl WL, et al. Interleukin-6 in the injured patient marker of injury or mediator of inflammation? *Ann Surg*. 1996;224(5):647–664.
14. Takahashi W, et al. Interleukin-6 levels act as a diagnostic marker for infection and a prognostic marker in patients with organ dysfunction in intensive care units. *Shock*. 2016;46(3):254–260.
15. Kruttgen A, Rose-John S. Interleukin-6 in sepsis and capillary leakage syndrome. *J Interferon Cytokine Res*. 2012;32(2):60–65.
16. Eulenfeld R, et al. Interleukin-6 signalling: more than Jaks and STATs. *Eur J Cell Biol*. 2012;91(6–7):486–495.
17. Babon JJ, et al. Inhibition of IL-6 family cytokines by SOCS3. *Semin Immunol*. 2014;26(1):13–19.
18. Harrison DA. The Jak/STAT pathway. *Cold Spring Harb Perspect Biol*. 2012;4(3):a011205.
19. Villarino AV, et al. Mechanisms and consequences of Jak-STAT signaling in the immune system. *Nat Immunol*. 2017;18(4):374–384.
20. Carow B, Rottenberg ME. SOCS3, a major regulator of infection and inflammation. *Front Immunol*. 2014;5:58.
21. Hou T, et al. Roles of IL-6-gp130 signaling in vascular inflammation. *Curr Cardiol Rev*. 2008;4(3):179–192.
22. Gurkan OU, et al. Interleukin-6 mediates pulmonary vascular permeability in a two-hit model of ventilator-associated lung injury. *Exp Lung Res*. 2011;37(10):575–584.
23. Strippoli R, et al. Amplification of the response to Toll-like receptor ligands by prolonged exposure to interleukin-6 in mice: implication for the pathogenesis of macrophage activation syndrome. *Arthritis Rheum*. 2012;64(5):1680–1688.
24. Wei LH, et al. The role of IL-6 trans-signaling in vascular leakage: implications for ovarian hyperstimulation syndrome in a murine model. *J Clin Endocrinol Metab*. 2013;98(3):E472–E484.
25. Zhang J, et al. Anti-IL-6 neutralizing antibody modulates blood-brain barrier function in the ovine fetus. *FASEB J*. 2015;29(5):1739–1753.
26. Alsaffar H, et al. Interleukin-6 promotes a sustained loss of endothelial barrier function via Janus kinase-mediated STAT3 phosphorylation and de novo protein synthesis. *Am J Physiol Cell Physiol*. 2018;314(5):C589–C602.
27. Valle ML, et al. Inhibition of interleukin-6 trans-signaling prevents inflammation and endothelial barrier disruption in retinal endothelial cells. *Exp Eye Res*. 2019;178:27–36.

28. Yun JH, et al. Endothelial STAT3 activation increases vascular leakage through downregulating tight junction proteins: implications for diabetic retinopathy. *J Cell Physiol*. 2017;232(5):1123–1134.
29. Maruo N, et al. IL-6 increases endothelial permeability in vitro. *Endocrinology*. 1992;131(2):710–714.
30. Desai TR, et al. Interleukin-6 causes endothelial barrier dysfunction via the protein kinase C pathway. *J Surg Res*. 2002;104(2):118–123.
31. Payne S, et al. Endothelial-specific Cre mouse models. *Arterioscler Thromb Vasc Biol*. 2018;38(11):2550–2561.
32. Huet O, et al. Ensuring animal welfare while meeting scientific aims using a murine pneumonia model of septic shock. *Shock*. 2013;39(6):488–494.
33. Shrum B, et al. A robust scoring system to evaluate sepsis severity in an animal model. *BMC Res Notes*. 2014;7:233.
34. Mai SHC, et al. Body temperature and mouse scoring systems as surrogate markers of death in cecal ligation and puncture sepsis. *Intensive Care Med Exp*. 2018;6(1):20.
35. Cunningham PN, et al. Acute renal failure in endotoxemia is caused by TNF acting directly on TNF receptor-1 in kidney. *J Immunol*. 2002;168(11):5817–5823.
36. Gluba A, et al. The role of Toll-like receptors in renal diseases. *Nat Rev Nephrol*. 2010;6(4):224–235.
37. Craciun FL, et al. Early murine polymicrobial sepsis predominantly causes renal injury. *Shock*. 2014;41(2):97–103.
38. Siewert E, et al. Different protein turnover of interleukin-6-type cytokine signalling components. *Eur J Biochem*. 1999;265(1):251–257.
39. Sasaki A, et al. The N-terminal truncated isoform of SOCS3 translated from an alternative initiation AUG codon under stress conditions is stable due to the lack of a major ubiquitination site, Lys-6. *J Biol Chem*. 2003;278(4):2432–2436.
40. Liu Z, et al. Systematic comparison of 2A peptides for cloning multi-genes in a polycistronic vector. *Sci Rep*. 2017;7(1):2193.
41. Balwierz PJ, et al. ISMARA: automated modeling of genomic signals as a democracy of regulatory motifs. *Genome Res*. 2014;24(5):869–884.
42. Szklarczyk D, et al. STRING v11: protein-protein association networks with increased coverage, supporting functional discovery in genome-wide experimental datasets. *Nucleic Acids Res*. 2019;47(D1):D607–D613.
43. Folco EJ, et al. Neutrophil extracellular traps induce endothelial cell activation and tissue factor production through interleukin-1α and cathepsin G. *Arterioscler Thromb Vasc Biol*. 2018;38(8):1901–1912.
44. O'Brien XM, et al. Consequences of extracellular trap formation in sepsis. *Curr Opin Hematol*. 2017;24(1):66–71.
45. Endemann DH, Schiffrin EL. Endothelial dysfunction. *J Am Soc Nephrol*. 2004;15(8):1983–1992.
46. Coletta C, et al. Endothelial dysfunction is a potential contributor to multiple organ failure and mortality in aged mice subjected to septic shock: preclinical studies in a murine model of cecal ligation and puncture. *Crit Care*. 2014;18(5):511.
47. Perico L, et al. Immunity, endothelial injury and complement-induced coagulopathy in COVID-19. *Nat Rev Nephrol*. 2021;17(1):46–64.
48. Nägele MP, et al. Endothelial dysfunction in COVID-19: current findings and therapeutic implications. *Atherosclerosis*. 2020;314:58–62.
49. Hierholzer C, et al. Activation of STAT proteins in the lung of rats following resuscitation from hemorrhagic shock. *Arch Orthop Trauma Surg*. 1998;117(6–7):372–375.
50. Suzuki S, et al. Phosphorylation of signal transducer and activator of transcription-3 (Stat3) after focal cerebral ischemia in rats. *Exp Neurol*. 2001;170(1):63–71.
51. Schaefer LK, et al. Constitutive activation of Stat3alpha in brain tumors: localization to tumor endothelial cells and activation by the endothelial tyrosine kinase receptor (VEGFR-2). *Oncogene*. 2002;21(13):2058–2065.
52. Yang XP, et al. Signal transducer and activator of transcription 3alpha and specificity protein 1 interact to upregulate intercellular adhesion molecule-1 in ischemic-reperfused myocardium and vascular endothelium. *Arterioscler Thromb Vasc Biol*. 2005;25(7):1395–1400.
53. Wang XF, et al. Association of pSTAT3-VEGF signaling pathway with peritumoral edema in newly diagnosed glioblastoma: an immunohistochemical study. *Int J Clin Exp Pathol*. 2014;7(9):6133–6140.
54. Severgnini M, et al. Activation of the STAT pathway in acute lung injury. *Am J Physiol Lung Cell Mol Physiol*. 2004;286(6):L1282–L1292.
55. Rummel C, et al. Nuclear translocation of the transcription factor STAT3 in the guinea pig brain during systemic or localized inflammation. *J Physiol*. 2004;557(Pt 2):671–687.
56. Rummel C, et al. Nuclear STAT3 translocation in guinea pig and rat brain endothelium during systemic challenge with lipopolysaccharide and interleukin-6. *J Comp Neurol*. 2005;491(1):1–14.
57. Damm J, et al. The putative JAK-STAT inhibitor AG490 exacerbates LPS-fever, reduces sickness behavior, and alters the expression of pro- and anti-inflammatory genes in the rat brain. *Neuropharmacology*. 2013;71:98–111.
58. Vallieres L, Rivest S. Regulation of the genes encoding interleukin-6, its receptor, and gp130 in the rat brain in response to the immune activator lipopolysaccharide and the proinflammatory cytokine interleukin-1beta. *J Neurochem*. 1997;69(4):1668–1683.
59. Verbsky JW, et al. Expression of Janus kinase 3 in human endothelial and other non-lymphoid and non-myeloid cells. *J Biol Chem*. 1996;271(24):13976–13980.
60. Pena G, et al. Unphosphorylated STAT3 modulates alpha 7 nicotinic receptor signaling and cytokine production in sepsis. *Eur J Immunol*. 2010;40(9):2580–2589.
61. Pena G, et al. JAK2 inhibition prevents innate immune responses and rescues animals from sepsis. *J Mol Med (Berl)*. 2010;88(8):851–859.
62. Uckun FM, et al. Anti-inflammatory activity profile of JANEX-1 in preclinical animal models. *Bioorg Med Chem*. 2008;16(3):1287–1298.
63. Hui L, et al. Inhibition of Janus kinase 2 and signal transduction and activator of transcription 3 protect against cecal ligation and puncture-induced multiple organ damage and mortality. *J Trauma*. 2009;66(3):859–865.
64. Lee JE, et al. Janex-1, a JAK3 inhibitor, ameliorates tumor necrosis factor-α-induced expression of cell adhesion molecules and improves myocardial vascular permeability in endotoxemic mice. *Int J Mol Med*. 2012;29(5):864–870.
65. Welte T, et al. STAT3 deletion during hematopoiesis causes Crohn's disease-like pathogenesis and lethality: a critical role of STAT3 in innate immunity. *Proc Natl Acad Sci U S A*. 2003;100(4):1879–1884.
66. Laouar Y, et al. STAT3 is required for Flt3L-dependent dendritic cell differentiation. *Immunity*. 2003;19(6):903–912.

67. Wang M, et al. Endothelial STAT3 plays a critical role in generalized myocardial proinflammatory and proapoptotic signaling. *Am J Physiol Heart Circ Physiol*. 2007;293(4):H2101–H2108.
68. Kano A, et al. Endothelial cells require STAT3 for protection against endotoxin-induced inflammation. *J Exp Med*. 2003;198(10):1517–1525.
69. Zhang X, et al. Endothelial STAT3 is essential for the protective effects of HO-1 in oxidant-induced lung injury. *FASEB J*. 2006;20(12):2156–2158.
70. Miller AM, et al. Anti-inflammatory and anti-apoptotic roles of endothelial cell STAT3 in alcoholic liver injury. *Alcohol Clin Exp Res*. 2010;34(4):719–725.
71. Roberts AW, et al. Placental defects and embryonic lethality in mice lacking suppressor of cytokine signaling 3. *Proc Natl Acad Sci U S A*. 2001;98(16):9324–9329.
72. White CA, Nicola NA. SOCS3: an essential physiological inhibitor of signaling by interleukin-6 and G-CSF family cytokines. *JAKSTAT*. 2013;2(4):e25045.
73. Iskander KN, et al. Cecal ligation and puncture-induced murine sepsis does not cause lung injury. *Crit Care Med*. 2013;41(1):159–170.
74. Nakazawa D, et al. Histones and neutrophil extracellular traps enhance tubular necrosis and remote organ injury in ischemic AKI. *J Am Soc Nephrol*. 2017;28(6):1753–1768.
75. Kim SY, et al. Blood-brain barrier dysfunction-induced inflammatory signaling in brain pathology and epileptogenesis. *Epilepsia*. 2012;53(suppl 6):37–44.
76. Girard TD, et al. Delirium as a predictor of long-term cognitive impairment in survivors of critical illness. *Crit Care Med*. 2010;38(7):1513–1520.
77. Cunningham C. Systemic inflammation and delirium: important co-factors in the progression of dementia. *Biochem Soc Trans*. 2011;39(4):945–953.
78. Sonneville R, et al. Understanding brain dysfunction in sepsis. *Ann Intensive Care*. 2013;3(1):15.
79. Taccone FS, et al. Brain perfusion in sepsis. *Curr Vasc Pharmacol*. 2013;11(2):170–186.
80. Pandharipande PP, et al. Long-term cognitive impairment after critical illness. *N Engl J Med*. 2013;369(14):1306–1316.
81. Colbert JF, Schmidt EP. Endothelial and microcirculatory function and dysfunction in sepsis. *Clin Chest Med*. 2016;37(2):263–275.
82. Ellis CG, et al. The microcirculation as a functional system. *Crit Care*. 2005;9(suppl 4):S3–S8.
83. Miranda M, et al. Microcirculatory dysfunction in sepsis: pathophysiology, clinical monitoring, and potential therapies. *Am J Physiol Heart Circ Physiol*. 2016;311(1):H24–H35.
84. Okajima K, et al. Plasma levels of soluble E-selectin in patients with disseminated intravascular coagulation. *Am J Hematol*. 1997;54(3):219–224.
85. Amalakuhan B, et al. Endothelial adhesion molecules and multiple organ failure in patients with severe sepsis. *Cytokine*. 2016;88:267–273.
86. Erikson K, et al. Retinal arterial blood flow and retinal changes in patients with sepsis: preliminary study using fluorescein angiography. *Crit Care*. 2017;21(1):86.
87. Backes Y, et al. Usefulness of suPAR as a biological marker in patients with systemic inflammation or infection: a systematic review. *Intensive Care Med*. 2012;38(9):1418–1428.
88. Gussen H, et al. Neutrophils are a main source of circulating suPAR predicting outcome in critical illness. *J Intensive Care*. 2019;7:26.
89. Sarhan J, et al. Constitutive interferon signaling maintains critical threshold of MLKL expression to license necroptosis. *Cell Death Differ*. 2019;26(2):332–347.
90. Schreiber A, et al. Necroptosis controls NET generation and mediates complement activation, endothelial damage, and autoimmune vasculitis. *Proc Natl Acad Sci U S A*. 2017;114(45):E9618–E9625.
91. Wang Y, et al. Ephrin-B2 controls VEGF-induced angiogenesis and lymphangiogenesis. *Nature*. 2010;465(7297):483–486.
92. Madisen L, et al. A robust and high-throughput Cre reporting and characterization system for the whole mouse brain. *Nat Neurosci*. 2010;13(1):133–140.
93. Yasukawa H, et al. IL-6 induces an anti-inflammatory response in the absence of SOCS3 in macrophages. *Nat Immunol*. 2003;4(6):551–556.
94. Scarfe L, et al. Transdermal measurement of glomerular filtration rate in mice. *J Vis Exp*. 2018;(140):58520.
95. Crampton SP, et al. Isolation of human umbilical vein endothelial cells (HUVEC). *J Vis Esp*. 2007;(3):183.
96. Gimbrone MA Jr., et al. Human vascular endothelial cells in culture: growth and DNA synthesis. *J Cell Biol*. 1974;60(3):673–684.
97. Jaffe EA, et al. Culture of human endothelial cells derived from umbilical veins. Identification by morphologic and immunologic criteria. *J Clin Invest*. 1973;52(11):2745–2756.
98. Stewart SA, et al. Lentivirus-delivered stable gene silencing by RNAi in primary cells. *RNA*. 2003;9(4):493–501.
99. Love MI, et al. RNA-Seq workflow: gene-level exploratory analysis and differential expression. *F1000Res*. 2015;4:1070.
100. Patro R, et al. Salmon provides fast and bias-aware quantification of transcript expression. *Nat Methods*. 2017;14(4):417–419.
101. Huber W, et al. Orchestrating high-throughput genomic analysis with Bioconductor. *Nat Methods*. 2015;12(2):115–121.
102. Soneson C, et al. Differential analyses for RNA-seq: transcript-level estimates improve gene-level inferences. *F1000Res*. 2015;4:1521.
103. Love MI, et al. Moderated estimation of fold change and dispersion for RNA-seq data with DESeq2. *Genome Biol*. 2014;15(12):550.
104. Edgar R, et al. Gene expression omnibus: NCBI gene expression and hybridization array data repository. *Nucleic Acids Res*. 2002;30(1):207–210.